

NUMERICAL SIMULATIONS OF ASTROPHYSICAL JETS FROM KEPLERIAN DISKS. I. STATIONARY MODELS

RACHID OUYED¹ AND RALPH E. PUDRITZ²

Department of Physics and Astronomy, McMaster University, Hamilton, Ontario L8S 4M1, Canada

Received 1996 July 12; accepted 1997 January 14

ABSTRACT

We present 2.5-dimensional time-dependent simulations of the evolution of nonrelativistic outflows from Keplerian accretion disks orbiting low-mass protostars or black holes accreting at sub-Eddington rates. The gas is injected at a very small speed ($v_{\text{inj}} = 10^{-3}v_K$) from the surface of the disk (a fixed boundary in our simulations) into a cold corona. The corona is in stable equilibrium and is supported by Alfvénic turbulent pressure. The initial magnetic field configuration in the corona is poloidal and is given by a potential field ($J = 0$). This configuration is extended smoothly into the disk where the toroidal magnetic field is taken to scale inversely with the disk radius. We present the analytical and the numerical approaches to our problem, as well as many results for a steady state simulation. We find that the gas is centrifugally accelerated through the Alfvén and the fast magnetosonic (FM) surfaces and collimated into cylinders parallel to the disk’s axis. The collimation of the outflow is due to the pinch force exerted by the dominant toroidal magnetic field generated by the outflow itself. Beyond the FM surface, we found that a “Hubble” flow is present; $v_z \propto z$. The velocities achieved in our simulations are of the order of 180 km s^{-1} for our standard young stellar object (a $0.5 M_\odot$ protostar) and of the order of 10^5 km s^{-1} for our standard active galactic nuclei (a $10^8 M_\odot$ black hole). Our jet solutions, dominated mainly by the poloidal kinetic energy ρv_p^2 , are very efficient in magnetically extracting angular momentum and energy from the disk. We find the ratio of the disk accretion rate to the wind mass flux rate to be of the order of $\dot{m}_a/\dot{m}_w \simeq 6.0$. We find that our stationary outflows have many similarities to steady state models of MHD disk winds.

Subject headings: accretion, accretion disks — galaxies: jets — methods: numerical — MHD — shock waves

1. INTRODUCTION

One of the fundamental questions raised by observations of astrophysical jets concerns the mechanism for initiating and driving the outflows. Among the scenarios currently being actively investigated are magnetohydrodynamic (MHD) models in which magnetized accretion disks, rotating around central objects (protostars, black holes, or white dwarfs), are involved. In general there exist two classes of models:

1. Winds emanating directly from the surface of the disk (Blandford & Payne 1982, hereafter BP82; Uchida & Shibata 1985, hereafter US85; Camenzid 1987; Pudritz & Norman 1986; Lovelace, Wang, & Sulkanen 1987; Heyvaerts & Norman 1989, hereafter HN89; Pelletier & Pudritz 1992, hereafter PP92; Appl & Camenzid 1992; Königl & Ruden 1993, to cite only a few). These can be divided into two general types of models: (a) the Uchida-Shibata wind (US85) with its “uncoiling spring” picture and (b) centrifugally driven wind (see, e.g., BP82; PP92) and its “bead on a rigid wire” picture. In the US85 model, the large-scale magnetic field is twisted by the rotation of a radially collapsing, non-Keplerian, accretion disk. The magnetic twist accumulates in the disk but eventually relaxes through the emission of large-amplitude, nonlinear, torsional Alfvén waves that propagate in bipolar directions

along the large-scale magnetic field lines. These waves eject the matter in surface layer of the disk, which leads to the formation of transient bipolar mass ejections. In the centrifugally driven disk-wind model, on the other hand, the gas is centrifugally flung out from the surface of a Keplerian disk if field lines thread the disk at an angle of 60° or less with respect to the disk surface (BP82). If r_0 is the field line’s footpoint at the disk surface and $r_A(r_0)$ is the corresponding Alfvén point, then one can show that the dynamics of such a wind is mainly controlled by the length of the magnetic lever arm $r_A(r_0)$. Beyond the Alfvén surface, the $\mathbf{J}_p \times \mathbf{B}_\phi$ force eventually dominates providing the collimation of the outflow.

2. The X-wind model, wherein the wind emanates from the point at which the disk corotates with its central magnetized star (Shu et al. 1994). These authors assumed that the closed magnetosphere connecting the central star and the disk becomes partly open. The excess angular momentum brought in through the disk is extracted by magnetocentrifugally driven winds that emanate from the inner edge of the disk and flow along the open magnetic field lines. Although Shu et al. did not show how the closed dipole field becomes open, recent two-dimensional numerical investigations by Hayashi (1996) have shown that the closed field lines become partially open through magnetic reconnection leading to the ejection of a cold wind. While such a scenario may be plausible for the case of protostars, it may be less relevant for jets from accreting black holes. That is, the X-wind model might not provide a universal model for explaining astrophysical jets. Furthermore, on galactic

¹ ouyed@physics.mcmaster.ca.

² pudritz@physics.mcmaster.ca.

scales, the recent observed correlation between *signatures* of accretion disks (veiling, UV excess, etc.) and outflow (Cabrit & André 1991; Edwards, Ray, & Mundt 1993) seems to point towards the disk wind scenario. That is, since the latter mechanism might explain the physics of such winds independently of the detailed nature of the central object (from active galactic nuclei, hereafter AGNs, to young stellar objects, hereafter YSOs), we decided to consider only the case of disk winds.

The theoretical work, mentioned above, focused on formation, evolution, and stability of hydromagnetic disk-winds in both self-similar and non-self-similar models. All of the analytical models to date are based on solutions to the *time-independent* equations. Therefore, important features observed in nature such as episodic outflows (Hartigan 1989; Hartigan, Raymond, & Meaburn 1990; Reipurth, Raga, & Heathcote 1992; Ray & Mundt 1993; Eislöffel & Mundt 1994; Davis et al. 1995) or the dynamics during the initiation of these winds cannot be investigated. A *time-dependent* approach to this problem is necessary, but because of the complexity of the MHD equations, direct numerical simulation is currently the only effective tool.

A few numerical simulations of axisymmetric magnetized flows from accretion disks have been computed for two classes of models. In the first class, one attempts to follow the internal dynamics of the disk (Shibata & Uchida 1986, hereafter SU86, Stone & Norman 1994, hereafter SN94). For models in which the accretion disks have sub-Keplerian rotation rates (SU86; BL95) or in which the Balbus-Hawley instability is present (SN94), the disk undergoes rapid radial collapse that generates a strong toroidal twist of the threading magnetic field. This is the “coiled spring” that propagates away from the disk as a transient, nonlinear torsional Alfvén wave and an associated burst of matter. These models have not been run long enough to establish whether or not a steady state ensues or whether such outbursts would continue over the timescales demanded by the observations. In the second class of models, one treats the disk as a boundary condition at the base of the wind without following its internal dynamics, assuming it is in Keplerian equilibrium (Bell & Lucek 1995, hereafter BL95; Ustyugova et al. 1995, hereafter U95). This allows one to isolate the physics of the formation of the jet for a well-defined set of conditions imposed at the base of the wind.

Here, we adopt this second approach and present 2.5-dimensional, high-resolution, numerical MHD simulations of the onset and collimation of outflows from the surface of a Keplerian accretion disk around a central object. In our first paper (Ouyed et al. 1997), we showed some of the basic results of our simulations, which consist of both stationary and episodic outflows. In this paper, we present the technical details as well as many new results of a magnetized disk model that leads to the eventual formation of a stationary disk wind. As in Ouyed et al. (1997), the disk is treated as a boundary condition at the base of the outflow and is kept in Keplerian rotation throughout the simulation. We present a detailed analysis of such winds. We employed the ZEUS-2D numerical code, which is a two-dimensional Eulerian *finite difference code*. We refer the reader to Stone & Norman (1992a, 1992b, hereafter SN92a and SN92b, respectively) for the details. We extended the code in order to allow us to set a stable initial equilibrium numerically without the use of a softening parameter and tested it. Fur-

thermore, an isotropic Alfvénic turbulence was added to the dynamics, which allowed a wider range of application of the code to the study of outflows. A complete analysis package, using SM graphics, was also written (and linked to the code). This tool turned out to be very useful in analyzing the physics involved in our simulations (Ouyed 1996).

Here we describe in detail the problems inherent to the initial setup as well as many results for a simulation that ultimately achieved steady state. The organization of this paper is as follows: in § 2, we introduce the reader to the dimensionless hydromagnetic wind equations used, and in § 3, we describe the initial setup, that is, the state of the initial equilibrium both analytically and numerically. We explain our extended version of the ZEUS-2D code in § 4 and how it deals with the numerical difficulties introduced by our initial equilibrium. In § 5, we present our results and the analysis package we use, followed by a discussion and conclusions in § 6.

2. BASIC EQUATIONS

We present a brief discussion of the equations, describing the physics of magnetized astrophysical flows and of accretion disks. We adopt cylindrical coordinates (r, ϕ, z) with the central object at the origin and take the z -axis to be perpendicular to the disk, such that the *surface* of the disk lies in the $z = 0$ plane of our coordinate system. In general, the equations to be solved are (infinite conductor)

$$\frac{\partial \rho}{\partial t} + \nabla \cdot (\rho \mathbf{v}) = 0, \quad (2.1)$$

$$\frac{\partial \mathbf{B}}{\partial t} - \nabla \times (\mathbf{v} \times \mathbf{B}) = 0, \quad (2.2)$$

$$\rho \left[\frac{\partial \mathbf{v}}{\partial t} + (\mathbf{v} \cdot \nabla) \mathbf{v} \right] + \nabla(p + p_A) + \rho \nabla \Phi - \mathbf{j} \times \mathbf{B} = 0, \quad (2.3)$$

$$\rho \left[\frac{\partial e}{\partial t} + (\mathbf{v} \cdot \nabla) e \right] + p(\nabla \cdot \mathbf{v}) = 0, \quad (2.4)$$

$$\nabla \cdot \mathbf{B} = 0, \quad (2.5)$$

where ρ is the density, p is the gas pressure, \mathbf{B} is the magnetic field, \mathbf{v} is the velocity, e is the internal energy, $\mathbf{j} = \nabla \times \mathbf{B}/4\pi$ is the current density, and p_A is the Alfvénic turbulent pressure³ that is expected to be present in any rotating, magnetized gas (Balbus & Hawley 1991).

The point mass gravitational potential is given by $\Phi = -GM/(r^2 + z^2)^{1/2}$. We made several restrictions. First, we assume ideal MHD in our simulations. We also assume that the gas is ideal and described by a polytropic equation

³ The Alfvénic turbulent pressure $p_A = |\delta \mathbf{B}|^2/8\pi$ is estimated from the time-averaged fluctuating Lorentz force $(\nabla \times \delta \mathbf{B}) \times \delta \mathbf{B}/4\pi$ (Dewar 1970). Dewar showed for Alfvénic waves of wavelength λ small compared to the variation of the background fluid, that such disturbances propagate adiabatically conserving wave action. They induce a radiation stress on the background fluid that is readily shown to behave as an isotropic wave pressure p_A . The source of such fluctuations and the role the corresponding isotropic pressure plays in our work is described in details in § 3.3.2.

TABLE 1
JET UNITS

Object	r_i	$v_{K,i}$ (km s ⁻¹)	$t_i \equiv \frac{1}{\Omega_{K,i}}$ (days)
YSOs	$3R_*$	$104.0 \frac{\sqrt{M/0.5 M_\odot}}{\sqrt{r_i/0.05 \text{ AU}}}$	$0.86 \frac{(r_i/0.05 \text{ AU})^{3/2}}{\sqrt{M/0.5 M_\odot}}$
AGNs ^a (pc).....	$10r_g = 10^{-4}M_8$	$6.7 \times 10^4 \sqrt{\frac{10r_g}{r_i}}$	$0.53M_8 \left(\frac{10r_g}{r_i}\right)^{3/2}$

^a $r_g = 2GM/c^2$ is the Schwarzschild radius. $10r_g$ is a fiducial radius interior within which relativistic effects cannot be neglected. M_8 is the central mass in units of $10^8 M_\odot$.

of state⁴ $p = K\rho^\gamma$, where K is the polytropic constant and γ is the polytropic exponent (which we have to distinguish from the adiabatic exponent γ_{ad}).⁵ Here we adopt $\gamma = 5/3$. We also ignore radiative transfer effects.

Our goal is to solve the system of equations above using the ZEUS-2D code (SN92a, SN92b). We extended the code in order to accommodate the demands of our simulations (§ 4).

2.1. Dimensionless Equations

We choose a dimensionless form for our equations such that the physical quantities are given in units of their values at the innermost radius of the accretion disk r_i (r_i could be defined as being the surface of the star, the magnetopause radius of a magnetized star and surrounding disk; or the last stable Keplerian-like orbit around a black hole for AGNs). The radial distance to the footpoint of a given field line on the disk is denoted r_0 . In general then, we define our dimensionless variables as

$$\begin{aligned} r' &= \frac{r}{r_i}, \quad z' = \frac{z}{r_i}, \quad v' = \frac{v}{v_{K,i}}, \quad \rho' = \frac{\rho}{\rho_i}, \\ B' &= \frac{B}{B_i}, \quad \Phi' = -\frac{1}{\sqrt{r'^2 + z'^2}}, \quad \nabla' = r_i \nabla, \end{aligned} \quad (2.6)$$

where $v_{K,i} = (GM/r_i)^{1/2}$ is the Kepler speed at r_i and B_i the poloidal field at r_i . Time is given in units of $t_i = r_i/v_{K,i}$ so that the dimensionless time is

$$\tau = \frac{t}{t_i} \quad (2.7)$$

(see Table 1). The results can therefore be scaled to a central object of any desired mass (see the example in Table 2).

⁴ Since we are assuming a polytropic relation for an ideal gas, this is equivalent to adopting a certain relation $e = e(p)$. This means that one fixes the internal energy instead of determining it by the energy equation. That is, we will not solve for the energy eq. (2.4) in this work (see § 4.2 for more details).

⁵ A polytropic change is defined to be a quasi-static change carried out in such a way that the derivative $c = dQ/dT$ (the “specific heat”) varies in a specified way throughout the change. For example, in an adiabatic change $c = 0$; hence an adiabat is a polytrope of zero specific heat (Chandrasekhar 1939). Since the entropy is simply defined as $dS = dQ/T$, then shocks (requiring $dS > 0$) are not allowed for adiabatic changes ($dS = dQ/T = 0$). In our case, by taking $c \neq 0$, we allow shocks to occur. The polytropic index is $\gamma = [(c_p - c)/(c_v - c)]$, where c_p and c_v are the specific heat at constant pressure and constant volume, respectively. It is only when $c = 0$ that $\gamma = \gamma_{\text{ad}} = c_p/c_v$ (see § 4.2 for more details).

Using these dimensionless quantities, the equation of motion becomes

$$\left[\frac{\partial \mathbf{v}'}{\partial \tau} + (\mathbf{v}' \cdot \nabla') \mathbf{v}' \right] = -\frac{1}{\delta_i} \frac{\nabla'(p' + p'_\Lambda)}{\rho'} - \nabla' \Phi' + \frac{2}{\delta_i \beta_i} \frac{\mathbf{J}' \times \mathbf{B}'}{\rho'}, \quad (2.8)$$

where we have introduced the parameters

$$\delta_i = \gamma \frac{v_{K,i}^2}{c_{s,i}^2}, \quad (2.9)$$

as the ratio of Kepler to thermal energy density, and

$$\beta_i = \frac{8\pi p_i}{B_i^2}. \quad (2.10)$$

as the ratio of the gas to the magnetic pressure in the corona, at the innermost radius of the disk.

In what follows, we present both the analytical and the numerical approaches for simulating a corona around the central object that is initially in stable equilibrium and in pressure balance with the disk surface. In general, then, we solve analytically for an initial equilibrium and test our extended version of the ZEUS-2D code to ensure that it conserves the equilibrium.

From now on, and for simplicity, we drop the primes keeping in mind that our quantities henceforth represent dimensionless variables.

3. INITIAL CONDITIONS

3.1. Hydromagnetic Corona

We are interested in solving the MHD equations for the region above the disk surface ($z > 0.0$), where we assume that $v_z = v_r = v_\phi = 0$. We assume, for simplicity and for clarity, that $B_\phi = 0$ in the corona and that the initial poloidal magnetic field in the disk corona threads the surface of the underlying disk. The state we consider is one that would be in hydrostatic balance in the gravitational field of the central object in the absence of rotation of the disk (the latter introduces a flux of torsional Alfvén waves and toroidal field into the corona that we study in our simulation).

TABLE 2
STANDARD UNITS

Central Object	Mass (M_\odot)	r_i (AU)	$v_{K,i}$ (km s ⁻¹)	t_i (days)
Protostar	0.5	0.04	120.0	0.6
Black hole.....	10^8	20.6	6.7×10^4	0.53

Equation (2.8) above becomes

$$0 = -\frac{1}{\delta_i} \frac{\nabla(p + p_A)}{\rho} - \nabla\Phi + \frac{2}{\delta_i B_i} \frac{\mathbf{J} \times \mathbf{B}}{\rho}. \quad (3.11)$$

It is still a difficult task to solve the equation because of the Lorentz term. *A self-similar configuration (see, e.g., BP82) has the disadvantage of being mathematically difficult to deal with when solving for the initial equilibrium because its associated Lorentz force does not vanish.* We therefore consider simpler initial magnetic configurations.

3.2. Initial Magnetic Configuration in Corona

In order to allow a simple, self-consistent, initial coronal state to be established, we consider initial configurations whose Lorentz force $\mathbf{J} \times \mathbf{B} = 0$. The two magnetic configurations we have chosen both have $\mathbf{J} = 0$, which is the simplest way of satisfying this condition. The next step consists in choosing an appropriate magnetic potential $\mathbf{A} = A_\phi \mathbf{e}_\phi$ because then the divergence-free condition for axisymmetric flows is automatically satisfied. In this scheme, the components of the magnetic field for axisymmetric MHD are

$$B_r = -\frac{\partial A_\phi}{\partial z} \quad \text{and} \quad B_z = \frac{1}{r} \frac{\partial r A_\phi}{\partial r}, \quad (3.12)$$

where A_ϕ is given in units of $r_i B_i$. Two particularly straightforward initial magnetic configurations are the following:

1. The uniform vertical field configuration defined by

$$A_\phi = r \quad (3.13)$$

whose associated field is $B_z = 2$ and $B_r = 0.0$.

2. The potential configuration,

$$A_\phi = \frac{\sqrt{r^2 + (z_d + z)^2} - (z_d + z)}{r}, \quad (3.14)$$

where from equation (3.12), $B_z = 1/[r^2 + (z_d + z)^2]^{1/2}$ and $B_r = \{1 - (z_d + z)/[r^2 + (z_d + z)^2]^{1/2}\}/r$ (z_d is the dimensionless disk thickness).

Such configurations reduce the momentum equation to

$$0 = -\frac{1}{\delta_i} \frac{\nabla(p + p_A)}{\rho} - \nabla\Phi. \quad (3.15)$$

One is left with the pressure and the Alfvénic turbulence as the main mechanisms to counterbalance gravity.

3.3. Hydrostatic Equilibrium

3.3.1. Hot Corona: $p_A = 0$

This case corresponds to the simplest possible equilibrium, wherein gravity is exactly balanced by the gas pressure, the hot corona. In this case, the solution of equation (3.15) is

$$\frac{h}{\delta_i} + \Phi = \text{const}, \quad (3.16)$$

where h is the dimensionless enthalpy of the gas with its usual definition $\gamma p/(\gamma - 1)\rho$. Taking $\rho = \rho_\infty$ (with $\Phi_\infty = 0$) at infinity, we get

$$\rho = \left[\frac{(\gamma - 1)\delta_i}{\gamma} \frac{1}{\sqrt{r^2 + z^2}} + \rho_\infty^{(\gamma-1)} \right]^{1/(\gamma-1)}. \quad (3.17)$$

Imposing the inner boundary condition $\rho(r = 1, z = 0) = 1$ (or in dimensional form, $\rho = \rho_i$ at $r = r_i$), we obtain the constraint

$$\delta_i = \frac{\gamma}{(\gamma - 1)} (1 - \rho_\infty^{(\gamma-1)}). \quad (3.18)$$

For a hot corona supported solely by thermal pressure then, we require

$$\delta_i \leq \frac{\gamma}{(\gamma - 1)} = \frac{5}{2}. \quad (3.19)$$

Estimating a fiducial value for δ_i , using $m_H c_s^2/2 = kT_i$ (T_i is the temperature of the corona at r_i) and the expression for $v_{K,i}$ given in Table 1, we obtain

$$\delta_i \simeq 100 \times \left(\frac{M}{0.5 M_\odot} \right) \left(\frac{10^5 \text{ K}}{T_i} \right) \left(\frac{0.05 \text{ AU}}{r_i} \right), \quad (3.20)$$

for a YSO, and similarly

$$\delta_i \simeq 100 \times M_8 \left(\frac{5 \times 10^9 \text{ K}}{T_i} \right) \left(\frac{10 r_g}{r_i} \right) \quad (3.21)$$

for a black hole, where M_8 is the mass of the black hole in units of $10^8 M_\odot$. That is, δ_i is of the order of 100 on the basis of coronal temperatures of the order of 10^5 K for YSOs and 5×10^9 K for the case of AGNs (both estimated in § 3.4.1).

The values estimated above reflect the need for another agent, besides thermal pressure, to provide the equilibrium. For high-mass protostars and for AGNs accreting at super-Eddington rates, one expects radiation pressure to provide the support needed for the equilibrium; however, since no radiation is present in our simulations, we cannot simulate such objects, and we are restricted to study low-mass protostars and AGNs accreting below the Eddington limit.

3.3.2. Cold Corona

Here, Alfvénic turbulence is the extra agent that provides the bulk of the support against gravity. The source of such turbulent motion is likely to be magnetic in origin. The operation of the Balbus-Hawley instability (Balbus & Hawley 1991, 1992) is generally believed to be a mechanism of creating disk turbulence. These Alfvén waves will propagate into the corona providing the perturbations. One of the attractions of this turbulence is that the associated density fluctuations $\delta\rho$ are zero, in the linear regime, so that even though the motions might be strongly supersonic, there will not be rapid dissipation through shock formation (Mestel 1989). The associated energy input need not to be as heat but may be as macroscopic kinetic energy (Dewar 1970; Shu, Adams, & Linzano 1987; McKee & Zweibel 1992; Zweibel & McKee 1995). This makes it straightforward to incorporate into the code (§ 4.2).

Magnetic turbulence is usually defined by $(\delta B)/B$ with a corresponding Alfvén velocity $v_T = \delta B/(4\pi\rho)^{1/2}$. The corresponding parameter that measures the ratio of the squares of the thermal to MHD turbulent velocities in the corona is

$$\beta_T = \frac{c_s^2}{v_T^2}. \quad (3.22)$$

For ease of implementation, we assumed that β_T is a constant so that p_A scales with the gas pressure. In this case, one

can introduce an effective enthalpy

$$h_{\text{eff}} = (c_s^2 + v_T^2) = \left(1 + \frac{1}{\beta_T}\right) c_s^2 \quad (3.23)$$

so that the equilibrium equation is

$$\nabla \left(\frac{h_{\text{eff}}}{\delta_i} + \Phi \right) = 0 \quad (3.24)$$

whose solution is now

$$\rho = \left\{ \rho_{\infty}^{(\gamma-1)} + \frac{(\gamma-1)}{\gamma} \frac{\delta_i}{[1 + (1/\beta_T)]} \frac{1}{\sqrt{r^2 + z^2}} \right\}^{1/(\gamma-1)} \quad (3.25)$$

with the inner boundary constraint (and with $\rho_{\infty} = 0$) implying that

$$\frac{\gamma}{(\gamma-1)} \frac{[1 + (1/\beta_T)]}{\delta_i} = 1. \quad (3.26)$$

The above equation allows us to estimate the turbulent pressure needed to support the corona for a given gas pressure. For a typical $0.5 M_{\odot}$ YSO, with $\delta_i \simeq 100$, we estimate a sound speed of the order of 15 km s^{-1} . That is, using equation (3.26) we find $\beta_T = 0.03$, which corresponds to a turbulence velocity of the order of $v_T = 50 \text{ km s}^{-1}$. Such values for turbulence are smaller than the line widths of the observed forbidden lines around YSOs (Ouyed & Pudritz 1994b). For the case of AGNs and for a typical $10^8 M_{\odot}$ black hole, we estimate a sound speed of the order of $8.6 \times 10^3 \text{ km s}^{-1}$ and a corresponding turbulence velocity of $3.1 \times 10^4 \text{ km s}^{-1}$.

Alfvén turbulence as described by Dewar (1970) is applicable only for wavelength much smaller than the scale we are simulating. Any super-Alfvénic fluctuations ($\delta v = v_T > v_A$) will rapidly decay through compressive shocks and will heat up the corona. One usually imposes the condition

$$\delta v = v_T \leq v_A \quad \text{or} \quad \beta_c \leq \beta_T. \quad (3.27)$$

Now the β corresponding to the mean magnetic field in the corona is not a constant in our model. However, a tractable analytical solution for the initial coronal structure requires that β_T is constant. Thus, the condition (3.27) is rewritten as

$$\bar{\beta}_c \leq \beta_T, \quad (3.28)$$

where $\bar{\beta}_c$ is the average coronal β . For our fiducial parameters, this implies that

$$\bar{\beta}_c \leq \beta_T \simeq 0.03. \quad (3.29)$$

It turned out that for our chosen magnetic configurations, sub-Alfvénic and super-Alfvénic turbulent regions coexist. While models of Alfvénic turbulence suggests that $\gamma = \frac{1}{2}$ for a pure nondamping gas (McKee & Zweibel 1992; Zweibel & McKee 1995), we choose $\gamma = 5/3$ because of the coronal heating arising from the expected dissipation in super-Alfvénic turbulent regions (which we do not explicitly simulate).

The coronal density distribution that we adopt in all our numerical simulations is ($\gamma = 5/3$ and $\rho_{\infty} \simeq 0$),

$$\rho = \left(\frac{1}{\sqrt{r^2 + z^2}} \right)^{3/2} \quad (3.30)$$

(note that this density structure has the same form as that expected for a collapsing isothermal corona; Shu 1977) with

$$\rho_i = \frac{\beta_i \delta_i}{2} \frac{B_i^2 / 4\pi}{v_{K,i}^2} \quad (3.31)$$

at r_i . The above expression can explicitly be written as

$$\rho_i = 3.74 \times 10^{-14} \beta_i \delta_i \left(\frac{B_i}{10 \text{ G}} \right)^2 \left(\frac{r_i}{0.05 \text{ AU}} \right) \times \left(\frac{0.5 M_{\odot}}{M} \right) \text{ g cm}^{-3}, \quad (3.32)$$

for YSOs, and

$$\rho_i = 9.01 \times 10^{-18} \beta_i \delta_i \left(\frac{B_i}{100 \text{ G}} \right)^2 \left(\frac{r_i}{10 r_G} \right) \text{ g cm}^{-3}, \quad (3.33)$$

for AGNs. The choice of 100 G for typical AGN coronal field is compatible with sub-Eddington luminosity (see § 5.4).

3.4. Conditions in the Underlying Disk Surface

The Keplerian accretion disk surface (the base of the corona) provides fixed boundary conditions and is defined in the $z < 0$ region. Here we have no feedback from the jet to the disk.⁶

3.4.1. Pressure Balance

The surface of the disk is placed in pressure balance with the atmosphere above. This implies that

$$p_d = p_{\text{eff}0} = \left(1 + \frac{1}{\beta_T}\right) p_0, \quad (3.34)$$

where the subscript “ d ” stands for disk and “ 0 ” for coronal quantities at $z = 0$. Using an adiabatic equation of state for the gas in the disk’s surface [$p_d = p_{d_i} (\rho_d / \rho_{d_i})^\gamma$], it is trivial to show that there must therefore exist a density jump across the disk surface of the order

$$\frac{\rho_d}{\rho_0} = \frac{\rho_{d_i}}{\rho_i} = \text{const} = \eta_i, \quad (3.35)$$

where η_i is our third free parameter. Furthermore, for an ideal gas, one can write equation (3.34) as

$$c_{s,d}^2 = \frac{\gamma-1}{\gamma} \frac{\delta_i}{\eta_i} \times c_{s,0}^2, \quad (3.36)$$

or

$$T_d = \frac{\gamma-1}{\gamma} \frac{\delta_i}{\eta_i} \times T_0, \quad (3.37)$$

⁶ The disk is undeniably important in providing the initial conditions at the base of the jet. That is, one cannot have a complete understanding of the dynamics of the jet without including the physics of the underlying disk. One has to match disk solutions to wind solutions, at the disk surface, to completely study the origin, evolution, and stability of jets. Such studies have been carried out by many authors (see, e.g., Königl 1989; Ferreira & Pelletier 1995; Wardle & Königl 1993; Li 1995) who derived some physical conditions required to launch the jet magnetically and to produce a super-Alfvénic wind. However, these studies had to assume stationarity and self-similarity in order to solve the full set of nonlinear differential equations. These assumptions prevent one from studying time-dependent jets

where $T_0 = T(r, z = 0)$ and

$$T(r, z) = \frac{1}{\sqrt{r^2 + z^2}}. \quad (3.38)$$

Thus, our pressure balance condition implies that the temperature at the surface of the disk scales with disk radius as

$$T_d = \frac{\gamma - 1}{\gamma} \frac{\delta_i}{\eta_i} \times \frac{1}{r}. \quad (3.39)$$

This is different from the $r^{-1/2}$ variation that fits the observed flat spectrum in CTTSs (Adams, Lada, & Shu 1987; Beckwith et al. 1990, for YSOs) or the $r^{-3/4}$ variation as derived from the theory of optically thick Keplerian accretion disks for both YSOs and AGNs (Frank, King, & Raine 1992).

The above equation relates the disk's temperature to the coronal temperature so that if we assume a typical disk thickness of $z_d \simeq 0.1$ ($\equiv \eta_i \simeq 100$),⁷ equation (3.39) implies

$$T_{d,i} \simeq \frac{2}{5} T_i. \quad (3.40)$$

3.4.2. Thin versus Thick Accretion Disk Models

For thin disks, the condition

$$c_{s,d} \ll v_K \quad (3.41)$$

is always satisfied, as long as

$$\eta_i \geq \frac{\gamma - 1}{\gamma} \delta_i \quad (3.42)$$

(from eq. [3.36]), since $c_{s,0} \ll v_K$. That is, the density jump is of the order of δ_i or more, applicable only for disks whose thickness is

$$z_d \leq \sqrt{\frac{\gamma}{(\gamma - 1)\delta_i}}. \quad (3.43)$$

Hence, if $\delta_i \simeq 100.0$, then $z_d \leq 0.1$ as expected for a thin Keplerian disk.

The theory of thin Keplerian disks, assuming they are optically thick, shows that the temperatures in the inner parts of the disk can be written as (Frank et al. 1992)

$$T_{d,i} = 4.1 \times 10^3 \left(\frac{\dot{m}_a}{10^{-6} M_\odot \text{ yr}^{-1}} \right)^{1/4} \left(\frac{M_*}{0.5 M_\odot} \right)^{1/4} \times \left(\frac{0.05 \text{ AU}}{r_i} \right)^{3/4} \text{ K} \quad (3.44)$$

for YSOs, and

$$T_{d,i} = 10^5 \left(\frac{\dot{m}_a}{0.2 M_\odot \text{ yr}^{-1}} \right)^{1/4} M_8^{1/4} \left(\frac{10 r_g}{r_i} \right)^{3/4} \text{ K} \quad (3.45)$$

for AGNs. That is, the typical inner disk temperatures in YSOs is of the order of 4000 K and of about 10^5 K in AGNs. While such disk models are appropriate for YSOs, they have difficulties for the case of AGNs, as explained below.

For the case of a black hole, the standard thin disk model above has a problem with the spectrum. Indeed, extensive observations of black hole systems by *Ginga*, *Granat*, and the *Compton Gamma Ray Observatory* (Johnson et al. 1994; Kinzer et al. 1994; Gilfanov et al. 1995, to cite only a few)

suggest radiation from an optically thin plasma with temperatures $T > 10^9$ K. This is much higher than the one given in equation (3.45). Inner disk temperatures of 10^9 – 10^{10} K arise naturally in the theory of geometrically thick, optically thin advective disks, however (Esin, Narayan, & Ostriker 1996). We will assume therefore that for AGNs, thick disks provide us with the fixed boundary at the base of the corona. Such disks may have considerable radial inflow speeds, but we ignore these in our simulations. Our chosen model is in agreement with the convective disk model, which is applicable only for black holes accreting at sub-Eddington rates (Esin et al. 1996).

From the above discussion and using equation (3.40), we estimate coronal temperatures of about 10^5 K for YSOs and about 5×10^9 K for AGNs. These values have been used in our estimate of δ_i in § 3.3.

3.4.3. The Disk's Current

Thus, the radial balance equation describing the surface of our Keplerian disk, for the configurations chosen, becomes

$$0 = \rho_d \frac{v_\phi^2}{r} - \rho_d \frac{\partial}{\partial r} (\Phi) - \frac{2}{\delta_i \beta_i} \frac{B_\phi}{4\pi} \frac{\partial}{\partial r} (r B_\phi) \quad (3.46)$$

in the r -direction. Thus, to be consistent, the last term in equation (3.46) must be unimportant. This can occur either because of weak toroidal fields ($B_\phi^2/8\pi \ll \rho v_\phi^2/2$) or when $B_\phi \propto 1/r$ for strong toroidal fields. In the first case, we ran simulations with $B_\phi = 0$ in the disk and found that B_ϕ is nevertheless generated in the corona by inertial effects (this production of B_ϕ at the base of the corona in turn generates a strong magnetic torque on the surface of the disk which then launches an outflow, as described in eqs. [5.69] and [5.70]). The coronal B_ϕ would propagate into the disk, leaving it with a nonzero toroidal field. Our boundary conditions do not allow such a wave to propagate into the disk, however. Thus, we anticipate that disks must have nonzero toroidal fields.

We model such a field as

$$B_\phi = \frac{\mu_i}{r}, \quad (3.47)$$

which is a current-free configuration (PP92), where

$$\mu_i = \frac{B_{\phi i}}{B_i} \quad (3.48)$$

is introduced as our fourth free parameter. For completeness, the mean field β of the gas in the disk is simply given as

$$\beta_d = \frac{(\gamma - 1)}{\gamma} \delta_i \beta_0. \quad (3.49)$$

For the potential configuration that we study in this paper,

$$\beta_0 \simeq \beta_i r_0^{-1/2}. \quad (3.50)$$

That is, β_d falls from the innermost value of $[(\gamma - 1)/\gamma] \delta_i \beta_i$ to an outermost value of $[(\gamma - 1)/\gamma] \delta_i \beta_i r_e^{-1/2}$. The disk radius at which β_d is unity is simply given as

$$1 = \frac{(\gamma - 1)}{\gamma} \delta_i \beta_i r_1^{-1/2} \quad (3.51)$$

or

$$r_1 = \left(\frac{2}{5} \delta_i \beta_i \right)^2. \quad (3.52)$$

Interior to r_1 , we expect both global and local modes of the

⁷ It is straightforward to show that $z_d = 1/(\eta_i)^{1/2}$.

BH instability to be present, while the linear stage of this instability will dominate in the regions exterior to r_1 (Balbus & Hawley 1991, 1992). But, again, because we treat the disk simply as a boundary condition at the base of the corona, we cannot study how the instability will affect the physics of the outflow.

3.4.4. The Magnetic Field of the Disk

The initial radial and vertical magnetic field components in the disk, defined by A_ϕ , are matched continuously and smoothly onto the field in the corona. That is, we avoid the presence of any kind of kink in the initial magnetic configurations that might introduce some undesired spurious effects. In the potential field configuration, this is true as long as

$$(z_d + z) > 0 \quad \text{for } z < 0. \quad (3.53)$$

To summarize this analytical part of the paper, we have solved for a cold corona in hydrostatic equilibrium. Such a corona is defined by the two free parameters δ_i and β_i . Underlying it is the surface of a Keplerian disk with which it is in pressure balance. The disk is in centrifugal balance and is defined by three free parameters: the density jump η_i , the azimuthal to the poloidal magnetic field ratio μ_i , and the injection velocity $v_{inj} \equiv v_p/v_K$, defined as the ratio of the poloidal to the Kepler speed in the disk. To be more concise, the parameters δ_i and μ_i prescribe the strength of the coronal poloidal and toroidal fields; δ_i , the thermal energy of the corona; and η_i and v_{inj} together determine the mass and momentum injection rate into the corona. Note that β_T is directly linked to δ_i via equation (3.26) and is not an independent parameter. That is, our initial setup is completely defined by a set of five free parameters, namely (δ_i , β_i , η_i , μ_i , and v_{inj}).

4. NUMERICAL APPROACH

4.1. The Finite Difference Grid in ZEUS-2D

Here, we briefly introduce the reader to the ZEUS-2D grid as it is important in understanding the following sections. We refer the reader to SN92 for more details.

In Figure 1 (adapted from SN92), we show the two-dimensional staggered grid used by ZEUS-2D. The “a” grid is defined by the coordinates $[x1_a(i), x2_a(j)]$, while the “b” grid coordinates $[x1_b(i), x2_b(j)]$ define the zone centers. g_2 , g_{31} , and g_{32} are the scale factor variables of the diagonal metric tensor that describes the particular orthogonal system of work (here, in cylindrical coordinates, $g_2 = 1$ and $g_{31} = g_{32} = r$). In such a mesh, the scalar variables (ρ , e) are “zone centered,” while the vector variables (v , B) are “face centered.” Thus, gradient components of zone-centered scalars are face-centered quantities, divergences of face-centered vectors are zone-centered, and curl components of face-centered vectors (e.g., the current density $\mathbf{J} = \nabla \times \mathbf{B}$) are “edge-centered.”

Note, too, that grid variables have specific locations attributed to them. Thus, $x1_a(i)$ is a face-centered quantity, while $dx1_a(i) = x1_a(i+1) - x1_a(i)$ is a zone-centered quantity, etc. In this scheme, the MHD equations can be differenced directly. All difference equations use the following nomenclature. The indices (i, j) denote the variable value at the (i, j)th zone located at one of the zone center, zone face, or zone edge as discussed above. The indices is and js stand for the starting indices with $[x1_a(is) = x2_a(js) = 0.0]$, at the

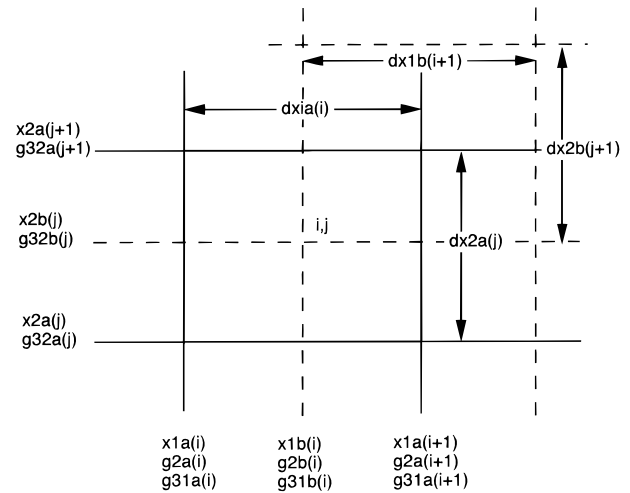


FIG. 1.—Coordinate grid definitions on the staggered grid used in ZEUS-2D: solid lines, “a-mesh”; dashed lines, “b-mesh.” g_2 , g_{31} , and g_{32} are the scale factor variables of the diagonal metric tensor that describes the particular orthogonal system of work (here, in cylindrical coordinates, $g_2 = 1$ and $g_{31} = g_{32} = r$).

origin of the a-mesh.

Two rows of “ghost” zones, defined beyond the computational domain [at ($is-1$), ($is-2$), ($js-1$), and ($js-2$)] are added along each boundary, as required by the piecewise parabolic advection (PPA) scheme implemented in ZEUS-2D. Values for the variables in the ghost zones are specified using boundary conditions appropriate to the geometry and physics of the problem being solved. Thus, evolution equations are not solved for the ghost zones. However, it is important to know that the ZEUS MHD algorithms will evolve the magnetic field components in a divergence-free manner, even in the ghost zones. This is an important point when considering the evolution of our initial magnetic configuration. In the “active” zones, the evolution equations are used to update the variables.

4.2. Setting Up the Initial Hydrostatic State

Our initial setup, while analytically simple, turned out to be a problem for the ZEUS-2D grid as described above. Our initial state solution requires that for the equilibrium to be achieved, the pressure gradient ∇p has to scale exactly with the potential gradient $\nabla \Phi$ owing to the point mass gravitational potential field. But since forces and density are defined at different locations on a staggered mesh, one has to use averaged densities in the momentum equations as depicted in equation (2.8). While such a procedure makes the code as general as possible, it presents a problem in our case. The difficulty is that because our density profile goes as $1/(r^2 + z^2)^{3/4}$, a simple two-point extrapolation scheme fails to calculate properly the density at the zone interface (where forces are located), destroying the initial equilibrium.

Usually, one deals with such a problem by adding a softening parameter. However, because our results changed significantly for slight variations of the softening parameter, such an approach is unreliable.⁸ Here, since the momentum

⁸ Bell & Lucek (1995) also came to the conclusion that the softening of the gravitational potential may be having a significant effect on the results. The effect of reducing their gravitational softening appears to favor the production of stronger jets.

equation we have finite differenced is

$$\left[\frac{\partial \mathbf{v}}{\partial \tau} + (\mathbf{v} \cdot \nabla) \mathbf{v} \right] = -\nabla(\rho^{(\gamma-1)} + \Phi) \quad (4.54)$$

(for polytropes), the interpolation problem is automatically taken care of, allowing easy implementation of the initial equilibrium. In addition, and for accuracy purposes, we have located the point mass gravitational potential Φ at zone centers⁹ in the b-mesh.

The equation above (applicable for simulating polytropic gases only) is different from the form used in ZEUS-2D. In particular, pressure does not appear explicitly in the momentum equation, making it independent of the energy equation, for which we do not solve here. It is straightforward to show that the thermodynamic entropy increases across shocks. However, one still needs to account for energy conservation by justifying some convenient energy source to take away the right amount of entropy. We showed that radiation from the forbidden-line emission detected in jets is a plausible candidate (Ouyed & Pudritz 1994a, 1994b). With our PDEs, we solve only for flows that possess no contact discontinuities (discontinuities moving with the flow) since we cannot have a jump in density without a jump in pressure.

Our approach preserves the initial equilibrium to machine roundoff accuracy. The avoidance of any gravitational *softening* parameter allows us to simulate outflows from the near vicinity of the central object. This last point is important for the understanding of the physics of astrophysical jets. Indeed, in Ouyed & Pudritz (1997), we show that because of the $1/r^{1/2}$ rotational (Keplerian) velocity law, the twisting of the magnetic field lines strongly increases as one approaches the surface of the central object. This creates a strong gradient in the generated toroidal magnetic field, which even opens up an initially vertical magnetic structure. Conditions favorable for ejection set themselves up automatically. The gas is centrifugally ejected from the portion of the disk surface where the magnetic field lines have opened to less than the critical angle ($\simeq 60^\circ$), as expected from the centrifugally driven wind theory.

Finally, having introduced an effective pressure, one also must ensure the accuracy and stability of the code. That is, one ensures that no signal shall cross more than half of any mesh zone in any given time step (physically, this is analogous to maintaining causality: each zone must know about each wave passing through it if the wave is to have any effect on it). This is done by taking into account the effective sound wave propagation in the Courant-Friedrich-Levy analysis¹⁰ (Courant & Friedrichs 1984). The feasibility and the conservation of the initial equilibrium with the extra term was successfully tested and satisfied to within machine roundoff error.

4.3. Initial Magnetic Configuration

We define A_ϕ at zone corners as required by the mesh staggering in ZEUS-2D. However, one must define the vector potential beyond the grid defined by ZEUS-2D. One

therefore needs to add an extra row and an extra column for A_ϕ .

A_ϕ is defined analytically in (§ 3.2) for the two configurations we are dealing with here. The potential configuration, as written in equation (3.14), presents a numerical difficulty; since A_ϕ is defined at the zone corners, one faces the problem of a singularity on the axis [$A_\phi \propto 1/x2a(j)$ with $x2a(js) = 0$]. Fortunately, we can deal with such a problem by using the stream function¹¹

$$\Phi_m = rA_\phi = \sqrt{r^2 + (z_d + z)^2} - (z_d + z), \quad (4.55)$$

with the field components given as

$$B_z = \frac{1}{r} \frac{\partial \Phi_m}{\partial r} \quad \text{and} \quad B_r = -\frac{1}{r} \frac{\partial \Phi_m}{\partial z}. \quad (4.56)$$

Because B_z is located at the face center in a zone, that is at $[x1a(i), x2b(j)]$, it has no singularity on the axis [since $x2b(js) \neq 0$]. As already explained in § 3.2, our configuration, extends continuously and smoothly into the disk ($z < 0$), eliminating any kinks that might introduce spurious current sheets in the initial setup. Numerically, since the disk's midplane is defined in the ghost zones, at $z = x1a(is-2)$, one has to set $z_d \geq x1a(is-2)$ artificially for condition (3.53) to be true. One has to remember that this is just a numerical artifact and that it does not change the way our physics is defined and set.

4.4. Parameters and Boundary Conditions

The set of five free parameters in our model consists of (δ_i , β_i , η_i , μ_i , $v_{in,j}$), and any given simulation will be assigned a set of these parameters. Since one of our main goals is to show the self-collimation of jets via self-generation of B_ϕ , we use open boundaries to avoid any artificial collimation owing to reflective boundaries. We use inflow boundary conditions (the values of all the variables in the ghost zones are held equal to a set of predetermined values, and outflow is not permitted) at the disk surface (except for the magnetic field for which we use open boundaries, so that it evolves through the $\nabla \cdot \mathbf{B} = 0$ constraint) and open outflow conditions (i.e., *zero normal gradient*) on the remaining boundaries. Along the axis of symmetry, coinciding with the disk axis, reflecting boundaries (i.e., *the normal components of velocity and magnetic field are reflected, while the tangential components are continuous*) are used. Because of the axisymmetry, we compute in only one quadrant. Figure 2 illustrates the initial setup and the open boundary mesh.

The conditions describing the central object and the accretion disk surface are set in the ghost zones and are fixed once and for all (they are fixed boundaries). In all our simulations, the gas is injected (inflow boundary) from the ghost zones into the active zones (the corona) at a velocity $v_p = 10^{-3} v_K$ (or $v_{in,j} = 10^{-3}$)¹² with $v_p \parallel \mathbf{B}_p$. Introducing the launching angle $\theta_0 = \tan(B_r/B_z)$, the velocity field in the ghost zone is

$$\mathbf{v} = (v_r, v_\phi, v_z) = [v_p \sin(\theta_0), v_K, v_p \cos(\theta_0)] \quad \text{if } r \geq 1 \quad (4.57)$$

$$= (0, 0, 0) \quad \text{if } r < 1. \quad (4.58)$$

⁹ In the original ZEUS-2D code, the point mass gravitational potential is defined by the central object located at the origin of the a-mesh $[x1a(is), x2a(js)]$.

¹⁰ This is set in the subroutines *nudt.src* and *setup.src* in ZEUS-2D code

¹¹ This configuration is similar to one given in Cao & Spruit (1994). It can be derived by taking $z_d = 1$. However, while their $z = 0$ surface corresponds to the disk's midplane, here it represents the surface of the disk.

¹² The injection velocity is taken to be the hundredth of the disk's sound speed.

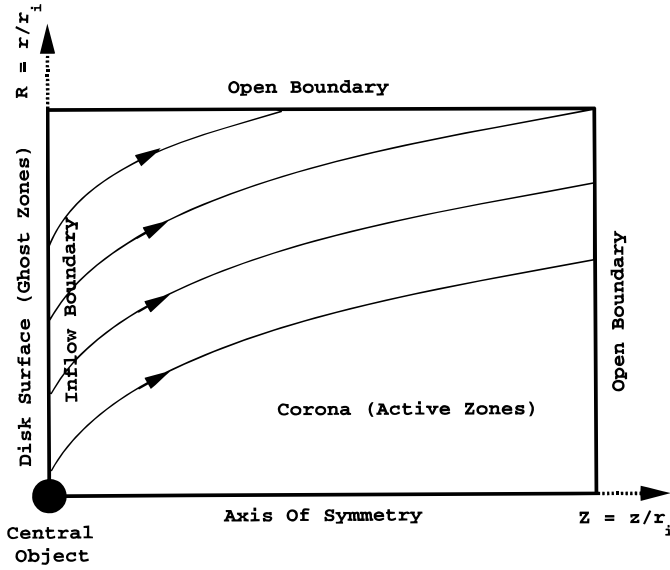


FIG. 2.—Setup of the numerical simulation. In this figure (and in all the figures), the axis of symmetry is plotted horizontally and the equatorial plane vertically. Note because of axisymmetry we compute in only one quadrant. The ghost zones ($z < 0.0$) define the surface of the Keplerian disk, while the active zones (which are evolved in time) define the corona. The magnetic field continues smoothly into the disk surface.

The second constraint incorporates a region interior to r_i (which might be an empty magnetosphere or simply a slowly rotating object) in which the disk is absent.

In the ghost zones, we also have

$$B_\phi = \frac{\mu_i}{r}, \quad (4.59)$$

while the poloidal field is given by equation (4.56) for $z < 0$. The disk's density is given as

$$\rho_d = \eta_i \rho_o = \eta_i r^{-3/2}. \quad (4.60)$$

4.5. Timescales

There are three important initial timescales defined at the disk's surface, where $t_x = r/v_x$, and v_x is the velocity of the wave considered. These are the Kepler time

$$\tau_K = \min \left(\frac{r}{v_K} \right), \quad (4.61)$$

the Alfvén time

$$\tau_A = \min \left(\frac{t_A}{t_i} \right) = \min \left(\frac{r}{v_A} \right), \quad (4.62)$$

and the magnetic braking time

$$\tau_B = \min \left(\frac{t_B}{t_i} \right) = \min \left(\eta_i \frac{r}{v_{A0}} \right) = \eta_i \times \tau_A, \quad (4.63)$$

which is the time it would take a torsional wave propagating onto the external medium to traverse an amount of material whose moment of inertia is the same as the moment of inertia of the disk (Mouschovias & Paleologou 1980, hereafter MP80). Note that because of the large density jump ($\eta_i \geq \delta_i = 100$), this time is unimportant in the dynamics (§ 5.2.1). The timescales above depend on the magnetic configuration chosen. However, it is straightforward to show

that

$$(\tau_K, \tau_A, \tau_B) = (1, \sqrt{\delta_i \beta_i / 2}, \eta_i \sqrt{\delta_i \beta_i / 2}), \quad (4.64)$$

where we naturally take $\min(\tau_K) = 1$ at $r = 1$.

5. NUMERICAL RESULTS: TESTING STEADY STATE MODELS

Here we present some preliminary results for a steady state simulation based on the potential field discussed in § 4.3. The parameters are

$$(\delta_i, \beta_i, \eta_i, \mu_i, v_{inj}) = (100.0, 1.0, 100.0, 1.0, 10^{-3}) \\ \Rightarrow (\tau_K, \tau_A, \tau_B) = (1.0, 7.07, 707.1). \quad (4.65)$$

The simulation was run in the domain $(z, r) = (80, 20)$ with a resolution of (500, 200) cells, for up to 500 time units ($< \tau_B$).

5.1. Steady State Theory

Before analyzing the above simulation, we present a brief introduction to the main results of the theory of steady state MHD winds. This will guide us in the choice of the appropriate diagnostics for steady state solutions. We remind the reader that all quantities are in their dimensionless form.

It is well known that, in the steady state limit, all equations (2.1)–(2.4) can be integrated once to yield the conservation of total specific energy $e(a)$ and angular momentum $l(a)$ along each field line ($2\pi a$ is the magnetic flux along a magnetic tube)

$$e(a) = \frac{v_p^2}{2} + \frac{v_\phi^2}{2} + h + \Phi - r \frac{B_\phi \Omega}{4\pi k} \quad (5.66)$$

$$l(a) = r v_\phi - \frac{r B_\phi}{4\pi k}, \quad (5.67)$$

where $k(a)$ is the mass flux per unit magnetic flux in the flow (also constant along a magnetic tube)

$$k(a) = \frac{\rho v_z}{B_z}. \quad (5.68)$$

To locate the position of the Alfvén point along a given field line, one needs to combine the equation for l and k above and the Alfvén critical condition $l(a) = \Omega r_A^2$ (see, e.g., BP82) to find that

$$\left[\left(\frac{r_A}{r_0} \right)^2 - 1 \right] = \frac{v_{A\phi}}{v_\phi} \frac{v_{Az}}{v_z} \Big|_{z=0}, \quad (5.69)$$

where

$$v_{Az} = \frac{B_z}{\sqrt{4\pi\rho}} \quad \text{and} \quad v_{A\phi} = \frac{B_\phi}{\sqrt{4\pi\rho}}. \quad (5.70)$$

The ratio r_A/r_0 is the so-called Alfvén lever arm, which defines the efficiency of the magnetic torque in extracting angular momentum through the surface of the disk. The quantities on the RHS are estimated at the disk surface, ($r, z = 0$).

5.1.1. Centrifugally Driven Winds

The mechanism for centrifugally driven winds, in the MHD limit, was first worked out by BP82, who constructed cold, time-independent, axisymmetric self-similar wind solutions above infinitely thin Keplerian disks. The gas is centrifugally flung out from the surface of a Keplerian accretion disk. Such winds can be launched if the field lines are inclined by no more than 60° from the surface of the disk

(we call this the launching condition). These wind solutions are controlled mainly by two dimensionless parameters that characterize the mass-loss rate (the κ of BP82) and the total specific angular momentum (their λ).¹³ In the BP82 scheme, it is easy to show that

$$\lambda = \left(\frac{r_A}{r_0}\right)^2 \quad \text{and} \quad \frac{B_\phi}{B_z} \Big|_{z=0} = -\kappa(\lambda - 1). \quad (5.71)$$

For a given field line, these two equations allow us to make contact with BP82 results (see § 5.3.1).

In their Figure 4, BP82 show the behavior of the physical quantities along a field line. Beyond the Alfvén surface (one of the wind's critical points), the $\mathbf{J}_p \times \mathbf{B}_\phi$ force (where B_ϕ is self-generated in the flow) eventually dominates providing the *self-collimation* of the outflow. The *final velocities* achieved by such winds are of the order of few times the Kepler velocity, along a given field line.

5.2. Evolution of the Outflow

The evolution of the flow can be described in three stages.

5.2.1. The Emission of Torsional Alfvén Waves

The early stage of the outflow is dominated by the propagation of a torsional Alfvén wave front from the disk surface. The *linear regime* of propagation of torsional waves is well presented in MP80. Briefly, the equation for propagation of linear torsional waves in the external medium can be shown to be

$$\frac{\partial^2 B_\phi}{\partial t^2} = v_{A, \text{ext}}^2 \frac{\partial^2 B_\phi}{\partial z^2}. \quad (5.72)$$

Waves are launched because of the existence of an initial gradient of B_ϕ in the z -direction. This arises from the fact that in our initial state, $B_\phi = 0$ in the corona while $B_\phi \propto 1/r$ in the disk. Now, because $v_{A, \text{ext}} \propto (r^2 + z^2)^{-1/4}$, torsional waves starting at different footpoints will travel into the corona at different velocities. This fact gives a conical shape to the Alfvén front, as is seen in the simulation.¹⁴ In our simulations, we can see these torsional Alfvén waves leaving the mesh while the outflow has not completely started yet. The magnetic configuration and the density distribution is still more or less in its initial state. As the gas becomes super-Alfvénic, it catches up with the Alfvén front and goes beyond it.

Note that in the classical scenario of the magnetic braking of an aligned rotator (which can be pictured as a rotating flat structure or flywheel that is threaded by straight magnetic field lines), the torsional waves propagate into the external medium, thereby slowing down the rotor. Physically, one expects such a flywheel to slow down significantly when the hydromagnetic waves propagating away from the cloud set into rotational motion an amount of external matter with moment of inertia equal to that of the cloud. This evolution of a disk is not expected in our simulation, since the central object forces the gas to remain in near-Kepler rotation at all times. For this reason, the conditions in the ghost zones (the disk surface) are set once and for all and are time independent (remember that the disk is just a boundary condition; it never evolves in time).

¹³ The requirement that their solution passes smoothly through the Alfvén critical point fixes the third parameter, namely the launching angle $\theta_{0, \text{BP}}$.

¹⁴ In the vertical field configuration, because $v_{A, \text{ext}} \propto (r^2 + z^2)^{3/8}$ we obtain a completely different wave front (Ouyed & Pudritz 1997).

However, as already mentioned in § 4.5, for the large density jump η_i expected for our accretion disk model, the timescale τ_B is very long, which reduces the braking effect in our simulations ($\tau_S < \tau_B$).

5.2.2. Interaction of the Outflow with the Corona

We find that an outflow is indeed launched from the disk surface. To illustrate the structure and dynamics of the outflow, we plot in Figure 3 the evolution of the density (*left-hand panels*) and of the toroidal magnetic field (*right-hand panels*). In Figure 4, we illustrate more of the dynamics of the jetlike outflow by plotting the density (*left-hand panels*) and the toroidal magnetic field (*right-hand panels*) along a cut parallel to the disk's axis. The cut is taken directly in Figure 3 at $r_0 = 5r_i$. The frames (for both figures) are for different time steps, which are $\tau = 0.0$, $\tau = 100.0$, $\tau = 200.0$, and $\tau = 400.0$ from top to bottom, respectively. The bow shock (at $\tau = 200$ in Fig. 3) traces the working surface of the outflow with respect to the undisturbed corona. There is also a highly collimated jetlike stream of gas that starts at the disk surface and terminates in a shock behind the working surface (at $\tau = 200$ in Fig. 4). The pivotal role that is played by the toroidal field is clearly shown. The outflow density along the outflow axis is clearly delimited by the region of strong toroidal field. Such features have been seen in pure MHD jet simulations (Clarke, Norman, & Burns 1986; Lind et al. 1989). The physical reason for this is the strong radial pinch force that is exerted toward the jet axis by the magnetic force arising through the combination of a dominant toroidal field and its associated current that flows primarily along the outflow axis.

In Figure 3, it is clearly seen that the jet is hollow (on radial scales $< r_i$), and no motion (outflow or inflow) is present within this hollow region. This is possible only under a strict initial equilibrium and is a consequence of our boundary condition that assumes the absence of a disk inside r_i . The density contrast between the interior of this region and the jet is of the order of 4. Such a region could provide a *channel* for the relativistic beams usually associated with the innermost regions of AGNs jets (see, e.g., Sol, Pelletier, & Asseo 1989; Pelletier & Sol 1992).

The thickness of the working surface of the jet (Fig. 4 at $\tau = 200$) is $3-4 r_i$. It is better seen in Figure 4 (at $\tau = 200$), where a density jump of about 4 is seen within the layer. The density features seen in Figure 3 (at $\tau = 300$) are transient, and the jet evolves quickly into the steady state.

Figure 5 shows the evolution of the initial potential magnetic field (*left-hand panels*) as well as of the launching angle (*right-hand panels*). The frames are for different time steps, which are $\tau = 0.0$, $\tau = 100.0$, $\tau = 200.0$, and $\tau = 400.0$ from top to bottom, respectively. As it evolves in time, the jet adjusts the launching angle along the disk surface (through the radial gradient of the generated B_ϕ) so as to make each field line go smoothly through the Alfvén and the FM critical points.

The poloidal velocity field (Fig. 6) shows that the highest speed gas is nearest the outflow axis, and farthest from the source!

5.2.3. Cylindrical Collimation

In the late stages of the outflow and beyond the Alfvén surface, the wound-up field collimates the gas toward the axis, as seen in the lower left-hand panel at $\tau = 400.0$. We found that our winds always collimate into cylinders along the symmetry axis at large distances from the source as

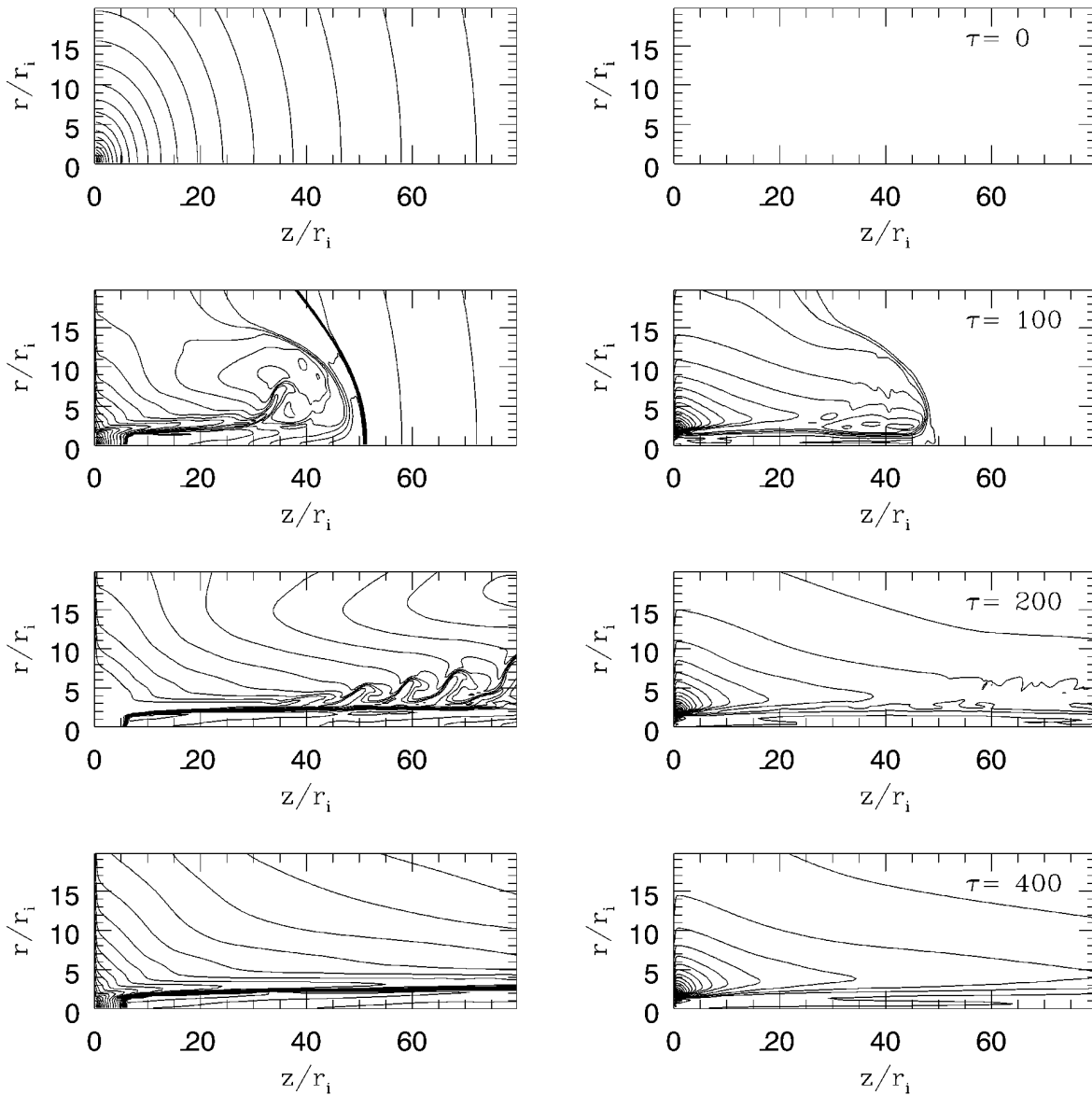


FIG. 3.—Evolution of the density (isocontours shown in the left-hand panels) and the toroidal magnetic field (isocontours shown in the right-hand panels). The initial density distribution, as given by eq. (3.30), is shown in the upper left-hand panel. Initially $B_\phi = 0.0$ in the corona (upper right-hand panel). The mesh is $(z \times r) = (80 \times 20)r_i$ with a resolution of (500×200) zones. Twenty logarithmically spaced contour lines are shown for the density, and 20 linearly spaced contours for B_ϕ . The evolution is shown at four different times: $\tau = 0$, $\tau = 100$, $\tau = 200$, and $\tau = 400$ from top to bottom.

predicted by HN89. Figure 7 shows the poloidal current density [$\tau = 400$ for a $(z \times r) = (100 \times 50)$ mesh]. Our final poloidal current is a nonvanishing one as required by HN89 solutions. When compared to the poloidal magnetic field lines, it is clearly seen that the jet is far from a force-free solution ($\mathbf{J}_p \parallel \mathbf{B}_p$). The current completes a circuit by flowing downward along the jet axis, radially outward through the accretion disk, and then upward along the flank of the bow shock, closing the circuit by returning to the outflow axis.

5.3. Steady State Solutions

A robust diagnostic for the existence of a steady state solution is to compute the angular momentum l and the mass flux-to-magnetic flux ratio k along any given field line. A steady state is achieved when these three quantities are constant along the field line. An example is given in Figure 8 for an inner field line ($r_0 \simeq r_i$). The dot represents the location of the Alfvén point, while the square is the FM

point, along the chosen field line. Note that beyond the FM surface, our solution seems to deviate away from the steady state but nonetheless it still oscillates around it.

Once the steady state is achieved, we estimate, from our numerical data, B_z , B_ϕ , and ρ at the footpoint of the given field line and compute the theoretical lever arm as given by equation (5.69). This is done for the simulation as a whole as shown in the lower panel of Figure 8, where we compare the Alfvén lever arms (filled hexagons) to the predictions from the steady state theory (squares). We find good agreement for streamlines that originate from the inner disk. Streamlines from the outer regions of the disk leave the mesh through the outer radial boundary before reaching the FM point, and this may affect the solution in the acceleration zone.

5.3.1. Driving Mechanism

A fundamental question arising from these results is to identify the force responsible for driving the mass outflow.

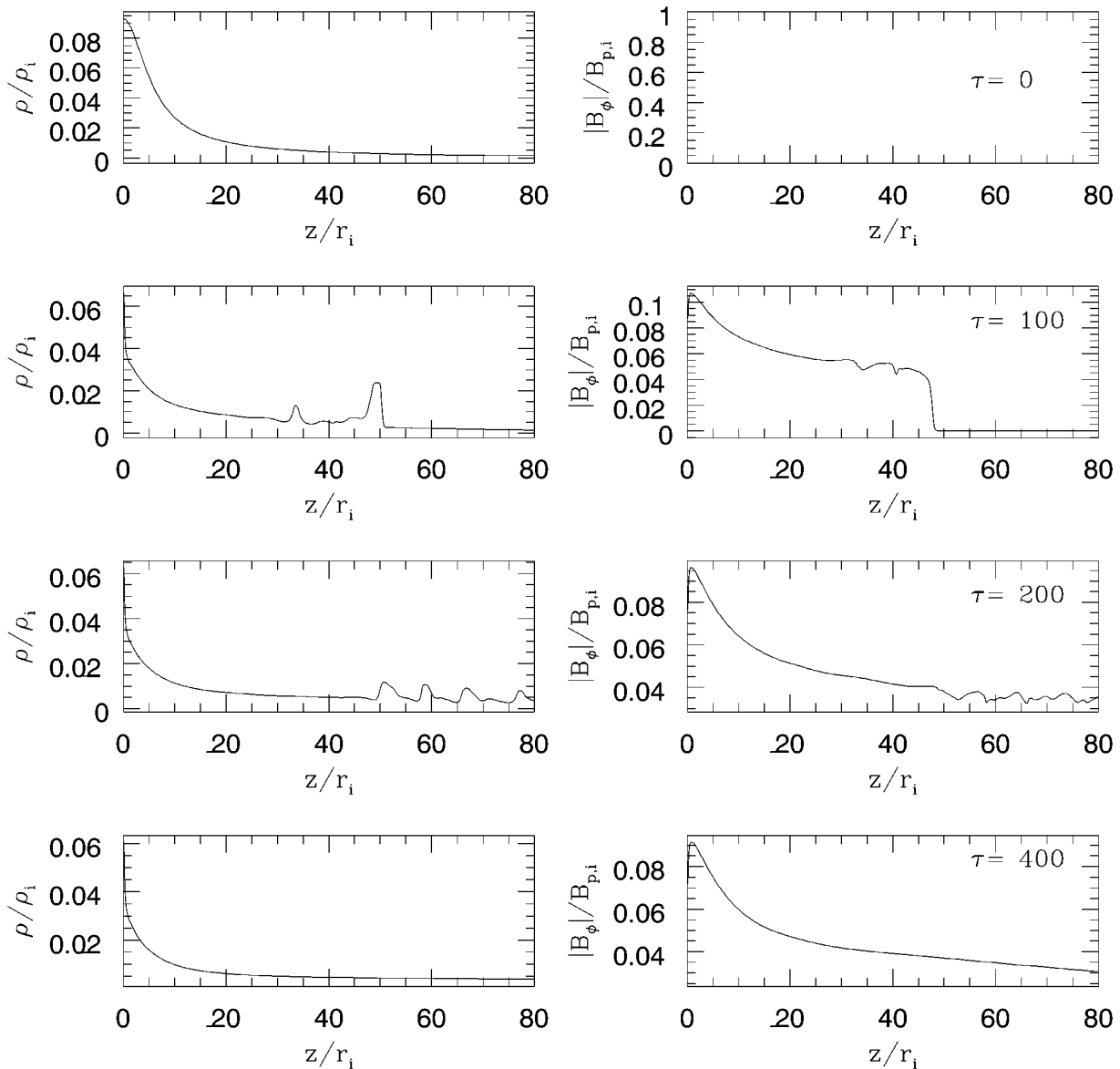


FIG. 4.—To complete Fig. 3, we plot here the density (*left-hand panels*) and $|B_\phi|$ (*right-hand panels*) along a cut parallel to the disk's axis. The cut is taken directly in Fig. 3 at $r_0 = 5r_i$ (as in Fig. 3, the panels are for four different times: $\tau = 0$, $\tau = 100$, $\tau = 200$, and $\tau = 400$ from top to bottom). This figure illustrates the values of the contour levels as well as the jet to the ambient density ratio during the evolution of the outflow.

We show in Ouyed et al. (1997) that the outflow is a result of the centrifugal wind mechanism. We showed the existence of an acceleration region, very close to the disk surface. The value of v_ϕ increases until the Alfvén critical point is reached as the matter is accelerated along the field lines by the magnetic stresses. Beyond the Alfvén point, the inertia of the matter dominates the azimuthal flow, and v_ϕ decreases as the matter attempts to conserve its angular momentum independently of the magnetic field. Beyond the Alfvén surface, the $\mathbf{J}_p \times \mathbf{B}_\phi$ force eventually dominates, which provides the collimation (where B_ϕ is self-generated in the flow). The final velocities achieved by such winds are of the order of 2 times the Kepler velocity, along a given field line (see Fig. 3 in Ouyed et al. 1997).

Estimating r_A/r_0 , B_ϕ/B_z , and the injection angle θ_0 (from our numerical data), for our chosen field line, we then use equations (5.71) to calculate the corresponding BP82 parameters κ and λ . In Figure 9, we plot the standard κ - λ graph (*upper panel*) and the κ - θ_0 graph (*lower panel*) with

the location of the launching angle θ_0 . In this simulation, the flow from the outer parts of the disk is particle-dominated ($\kappa \geq 1.0$ for the outer few field lines). This explains why the outer parts of the jet show less collimation compared to the inner part. It turns out that this is a boundary effect that can be taken care of by extending the size of the mesh (radially) and by increasing the computation time. We find that κ and λ can always be related by a simple relation. That is,

$$\lambda \simeq \frac{2.4}{\kappa^{2/3}}. \quad (5.73)$$

Simply put, since our launching angle becomes constant along the disk's surface (in the late stages of the simulation), the outflow manages to go smoothly through the Alfvén critical point and the FM point by finding the right combination of κ and λ at each disk's radius. The difference between the self-similar study (BP82 found $\lambda \simeq 1/\kappa$) and our

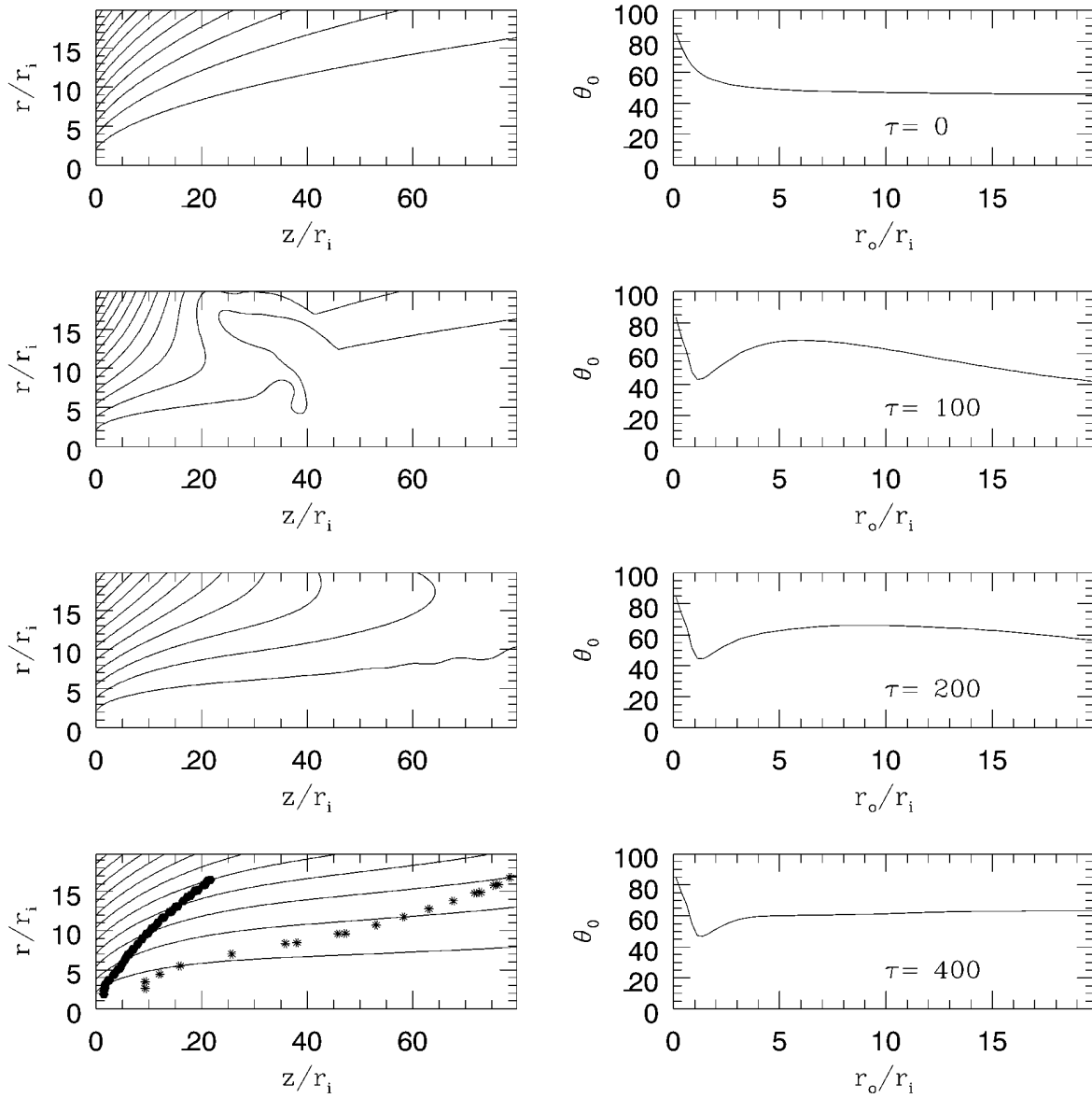


FIG. 5.—Evolution of the poloidal magnetic field (*left-hand panels*) and the launching angle at the disk's surface (*right-hand panels*). The initial magnetic potential configuration ($J = 0$), as given by (4.55), is shown in the upper left-hand panel. The mesh is $(z \times r) = (80 \times 20)r_i$ with a resolution of (500×200) zones. The evolution is shown at four different times: $\tau = 0$, $\tau = 100$, $\tau = 200$, and $\tau = 400$ from top to bottom. In the lower left-hand frame is displayed the location of the Alfvén critical surface (*filled hexagons*) and of the fast magnetosonic surface (*stars*).

result may be due to the different magnetic field distribution used; our outflow is not self-similar.

Finally, we find that the acceleration of material occurs in two separate spatial stages. In stage 1 (the region along a field line between the disk and the FM point), the centrifugal effect dominates. In stage 2 (the region beyond the FM point), a “Hubble flow” character of the flow with $v_z \propto z$ develops. While such behavior has been predicted for purely hydrodynamic flows (Raga & Kofman 1992), our solution predicts it for MHD flows as well. With a simple MHD approach, one can show that such a feature develops because the flow is highly super-Alfvénic and is cylindrically collimated (our case). Under these conditions, the force on the gas vanishes, $dv_z/dt \simeq 0$. The self-similar solution of this condition is just the Hubble flow. This is better illustrated in Figure 10, where we show the axial velocity along a cut taken parallel to the disk's axis, at $j = 40$ (here we have

extended the domain of simulation up to $z = 100.0$ and found that the so-called Hubble flow still persists).

5.4. Fluxes and Accretion Rates

In this scheme, mass flux is defined as

$$\dot{m}_w = \int_{r=0}^{r=r_{\max}} 2\pi\rho v_z dr. \quad (5.74)$$

For the protostellar case, mass flux is given in units of

$$\begin{aligned} \dot{m}_i &= 2\pi r_i^2 \rho_i V_{K,i} = 2.13\beta_i \delta_i \times 10^{-8} \left(\frac{M_*}{0.5 M_\odot} \right)^{-1/2} \\ &\times \left(\frac{r_i}{0.05 \text{ AU}} \right)^{5/2} \left(\frac{B_i}{10 \text{ G}} \right)^2 M_\odot \text{ yr}^{-1}. \end{aligned} \quad (5.75)$$

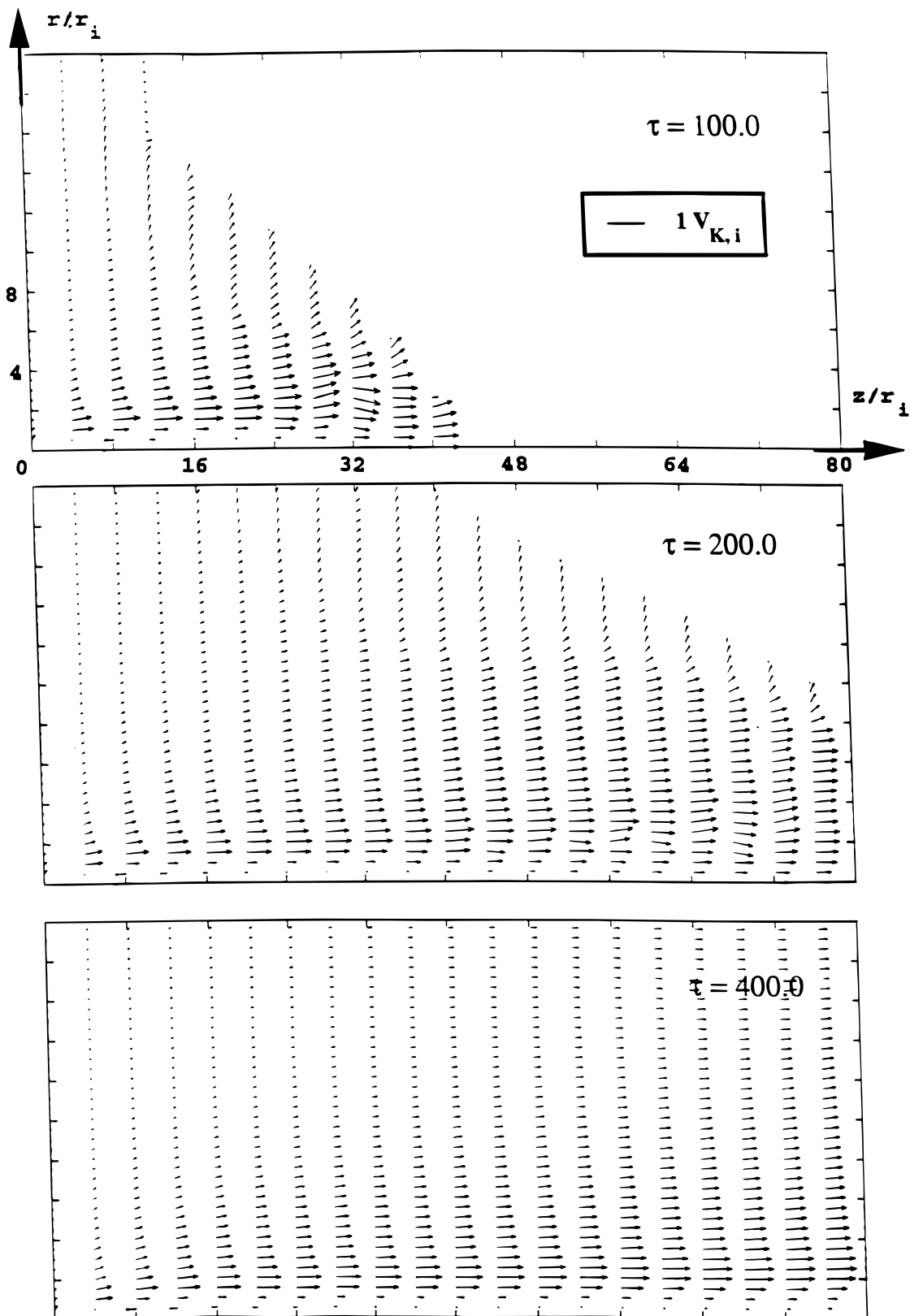


FIG. 6.—Poloidal vector velocity v_p at $\tau = 100$, $\tau = 200$, and $\tau = 400$, respectively, from top to bottom

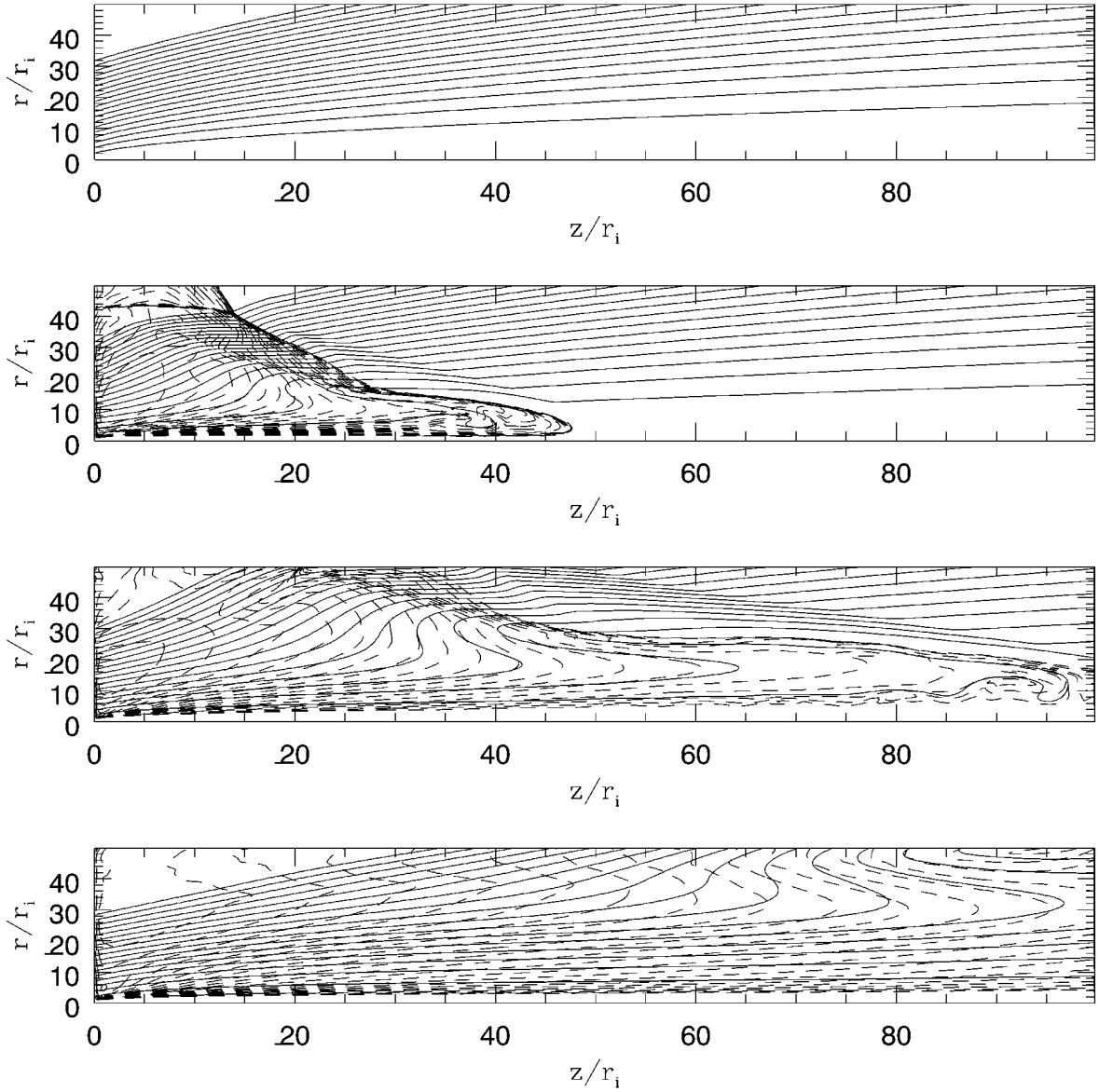


FIG. 7.—Isocontours of the poloidal current density (J_p ; dotted lines) and poloidal magnetic field lines (B_p ; solid lines) at time $\tau = 0$, $\tau = 100$, $\tau = 200$, and $\tau = 400$ from top to bottom, respectively. The jet is far from a force-free solution ($J_p \parallel B_p$). The current completes a circuit by flowing downward along the jet axis, radially outward through the accretion disk, and then upward along the flank of the bow shock, closing the circuit at the outflow axis.

The momentum flux is in units of

$$(\dot{m}v)_i = 2\pi r_i^2 \rho_i V_{K,i}^2 = 2.22\beta_i \delta_i \times 10^{-6} \left(\frac{r_i}{0.05 \text{ AU}} \right)^2 \times \left(\frac{B_i}{10 \text{ G}} \right)^2 M_\odot \text{ km s}^{-1} \text{ yr}^{-1} \quad (5.76)$$

while the kinetic flux is in units of

$$(\dot{m}v^2)_i = 2\pi r_i^2 \rho_i V_{K,i}^3 = 1.46\beta_i \delta_i \times 10^{31} \left(\frac{M_*}{0.5 M_\odot} \right)^{1/2} \times \left(\frac{r_i}{0.05 \text{ AU}} \right)^{3/2} \left(\frac{B_i}{10 \text{ G}} \right)^2 \text{ ergs s}^{-1}. \quad (5.77)$$

Similarly for AGNs, one gets the mass flux in units of

$$\dot{m}_i = 2\pi r_i^2 \rho_i V_{K,i} = 5.62\beta_i \delta_i \times 10^{-4} M_8^2 \left(\frac{r_i}{10 r_g} \right)^{5/2} \times \left(\frac{B_i}{10^2 \text{ G}} \right)^2 M_\odot \text{ yr}^{-1}. \quad (5.78)$$

The momentum flux is in units of

$$(\dot{m}v)_i = 2\pi r_i^2 \rho_i V_{K,i}^2 = 3.77\beta_i \delta_i \times 10^1 \left(\frac{r_i}{10 r_g} \right)^2 \times \left(\frac{B_i}{10^2 \text{ G}} \right)^2 M_\odot \text{ km s}^{-1} \text{ yr}^{-1}, \quad (5.79)$$

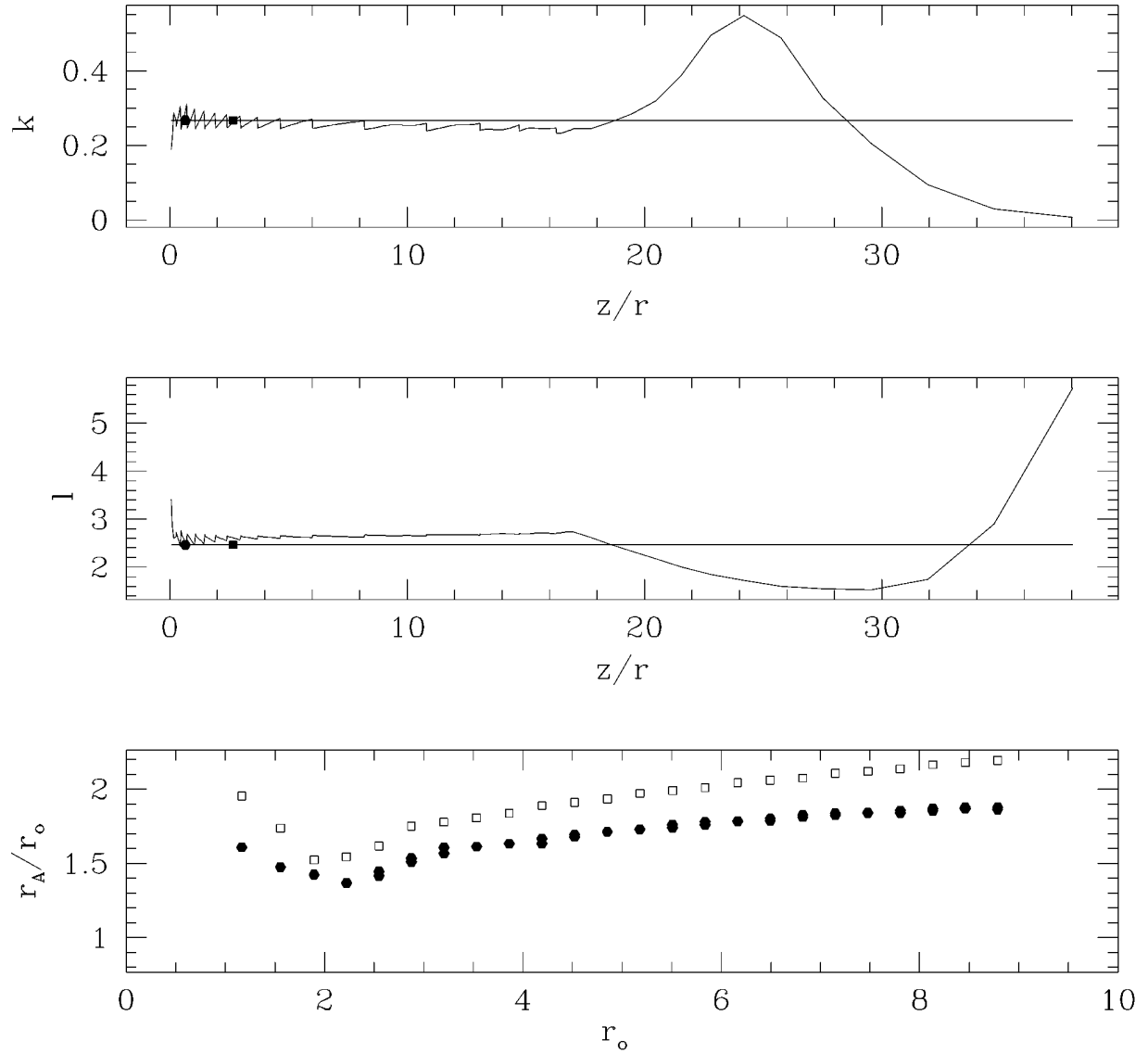


FIG. 8.—Steady state analysis of the innermost field line. This figure shows the mass to magnetic flux ratio k (*upper panel*) and the specific angular momentum l (*middle panel*) plotted against $z/r = \tan^{-1}(\psi)$, where ψ is the polar angle as measured from the origin of the coordinate system. The steady state theory (*solid line*) predicts that these two quantities are constant along a given field line. The filled dot and the filled square are the location of the Alfvén point and of the FM point, respectively, as found in our simulation, along the chosen field line. There is good agreement within the FM region. Beyond the FM point, the solution oscillates around the steady state behavior. In the lower frame, the Alfvén lever arms (r_A/r_0 , for a field line anchored at r_0 on the disk's surface), found in our simulation (*filled hexagons*) are compared to the prediction from the steady state theory (*squares*).

while the kinetic flux is in units of

$$(\dot{m}v^2)_i = 2\pi r_i^2 \rho_i V_{K,i}^3 = 1.6\beta_i \delta_i \times 10^{42} \left(\frac{r_i}{10r_g}\right)^{3/2} \times \left(\frac{B_i}{10^2 \text{ G}}\right)^2 \text{ ergs s}^{-1}. \quad (5.80)$$

We have used expressions (3.32) and (3.33) for ρ_i and replaced $v_{K,i}$ using Table 1.

For the case of AGNs, assuming an accretion efficiency ϵ , the accretion luminosity can be written as (see Frank et al. 1992, for example)

$$L_{\text{acc}} = \epsilon \dot{m}_a c^2. \quad (5.81)$$

Using the Eddington luminosity defined as $L_E = \dot{m}_E c^2$, where $\dot{m}_E = 4\pi G m_p / c \sigma_T$ is the Eddington accretion rate (σ_T is the Thomson cross section for electron scattering), we

find that

$$\frac{L_{\text{acc}}}{L_E} = \epsilon \frac{\dot{m}_a}{\dot{m}_E} = \epsilon \left(\frac{\dot{m}_a}{\dot{m}_w}\right) \left(\frac{\dot{m}_w}{\dot{m}_i}\right) \left(\frac{\dot{m}_i}{\dot{m}_E}\right). \quad (5.82)$$

For AGNs with sub-Eddington luminosities (§ 3.3.1), we require

$$\frac{L_{\text{acc}}}{L_E} = 2.81 \times 10^{-4} \left(\frac{\epsilon}{0.1}\right) \left(\frac{\dot{m}_a}{\dot{m}_w}\right) \left(\frac{\dot{m}_w}{\dot{m}_i}\right) \beta_i \delta_i M_8^{-3} \times \left(\frac{r_i}{10r_g}\right)^{5/2} \left(\frac{B_i}{10^2 \text{ G}}\right)^2 < 1, \quad (5.83)$$

where we have used equation (5.78) for m_i and $\dot{m}_E = 0.2M_8 M_\odot \text{ yr}^{-1}$. Since steady state theory predicts $\dot{m}_a/\dot{m}_w \simeq 10$ (BP82; PP92) and assuming $\dot{m}_w/\dot{m}_i < 1$, the above con-

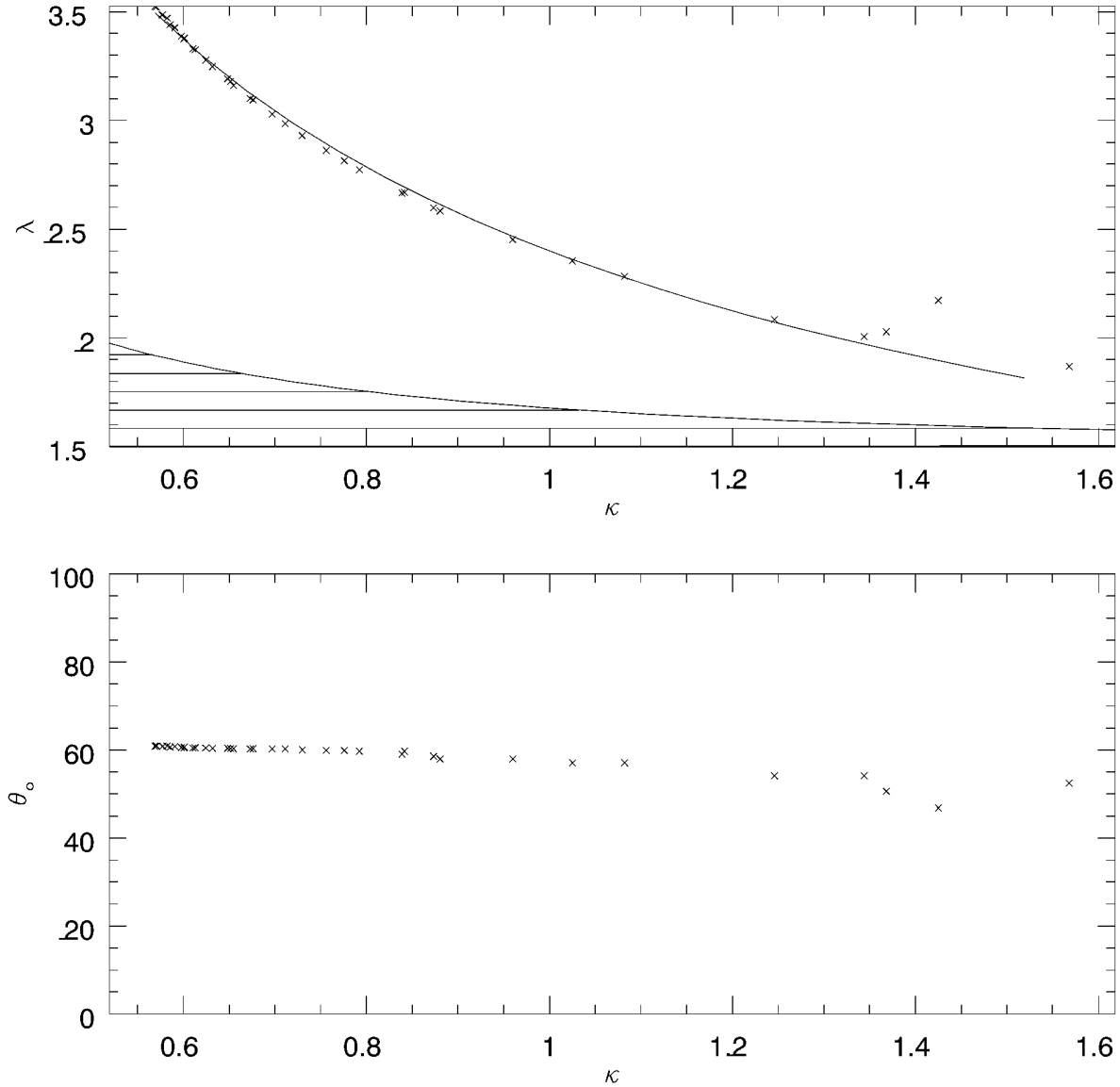


FIG. 9.—The κ - λ space (upper panel) and the κ - θ_0 space (lower panel) and the location of our solution, at $\tau = 400$. The two regimes of the jet, the magnetically dominated jet with $\kappa < 1$ (inner parts of the jet), and the particle-dominated jet with $\kappa \geq 1$ are shown. In the upper panel, the dashed area represents the sub-Alfvénic flows [$4\pi\rho v_p^2 < B_p^2$ or $\kappa\lambda(2\lambda - 3)^{1/2} < 1$]. The fitting curve is given by $\lambda = 2.4/\kappa^{2/3}$.

straint becomes

$$\frac{L_{\text{acc}}}{L_E} = 0.281 \left(\frac{\epsilon}{0.1} \right) M_8^{-3} \left(\frac{r_i}{10r_g} \right)^{5/2} \left(\frac{B_i}{10^2 \text{ G}} \right)^2 < 1, \quad (5.84)$$

for our fiducial parameters. This simple estimate shows why we take $B = 100$ G for sub-Eddington AGNs, in our model. We show from the following analysis that our simulations give values for \dot{m}_a/\dot{m}_w and \dot{m}_w/\dot{m}_i that are consistent with the above condition.

In Figure 11, we quantify the strength of the observed outflow. The solid line denotes the energy, momentum, and

TABLE 3
JET ENERGISTICS

Central Object	Mass (M_\odot)	\dot{m}_w ($M_\odot \text{ yr}^{-1}$)	$\dot{m}_w v$ ($M_\odot \text{ km s}^{-1} \text{ yr}^{-1}$)	$\frac{1}{2}\dot{m}_w v^2$ (ergs s $^{-1}$)
Protostar	0.5	9.1×10^{-7}	2.8×10^{-5}	8.0×10^{32}
Black hole.....	10^8	2.2×10^{-2}	7.5×10^2	1.2×10^{43}

mass fluxes across the inner ($z = 0.0$) boundary. The short dashed line denotes these fluxes across the outer radial boundary ($r = 20.0$). Finally, the dotted line denotes these fluxes across the outer axial boundary ($z = 80.0$). At later times, the fluxes in the outflow are comparable to the fluxes at the inner boundary. When given in cgs units (and assuming values for the free parameters appropriate to a protostellar disk and/or black holes), then the typical mass, momentum and energy flux rates are given in Table 3.

We further quantify the strength of our flow by plotting, in Figure 12, the bulk energies involved (integrated over the entire computing volume). While the upper panel shows that most of the magnetic energy is in the form of the toroidal ($B_\phi^2/8\pi$) form, the lower panel indicates that most of the kinetic energy is in the form of the bulk kinetic energy of the poloidal flow ($\rho v_p^2/2$). In general, our solution corresponds to flow in which most of the energy is shared between the bulk poloidal kinetic energy ($\frac{2}{3}$ of the total energy) and the toroidal magnetic energy (one-third of the total energy). If

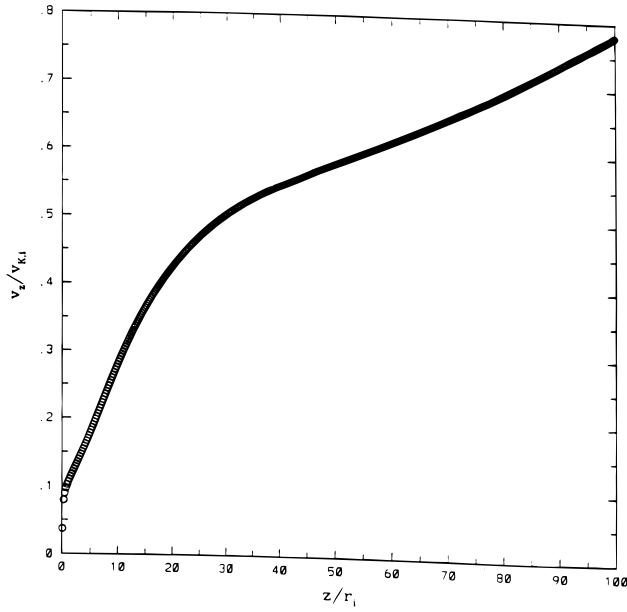


FIG. 10.—A cut parallel to the disk axis ($j = 40$) showing the velocity (v_z , in units of $v_{K,i}$) and its Hubble profile.

we assume that the total kinetic and magnetic power put into the jet is equal to half the total gravitational binding energy that can be released in the accretion disk [$L_w = \frac{1}{2}(GMM_a/r_i)$ from Pringle 1981; the other half of GMM_a/r_i being dissipated in the boundary layer; protostar or black hole], then we can write, in dimensionless form, that

$$3L_w = \frac{1}{2}\dot{m}_a, \quad (5.85)$$

where L_w is the total kinetic power of the flow from each surface of the disk, given in the upper panel of Figure 9. The factor 3 in front comes from the fact that one has to consider the two surfaces and the fact that $L_{\text{mag}} \simeq L_w/2$. Since $L_w \simeq \dot{m}_w = 0.3$ (see Fig. 11), we then find that,

$$\dot{m}_a \simeq 6.0\dot{m}_w. \quad (5.86)$$

Hence, only a fraction of the accreted gas needs to participate in the outflow, which clearly shows the high efficiency of centrifugally driven wind mechanism in magnetically extracting mass and energy from the disk. For AGNs and for our typical black hole, with an accretion efficiency ϵ of

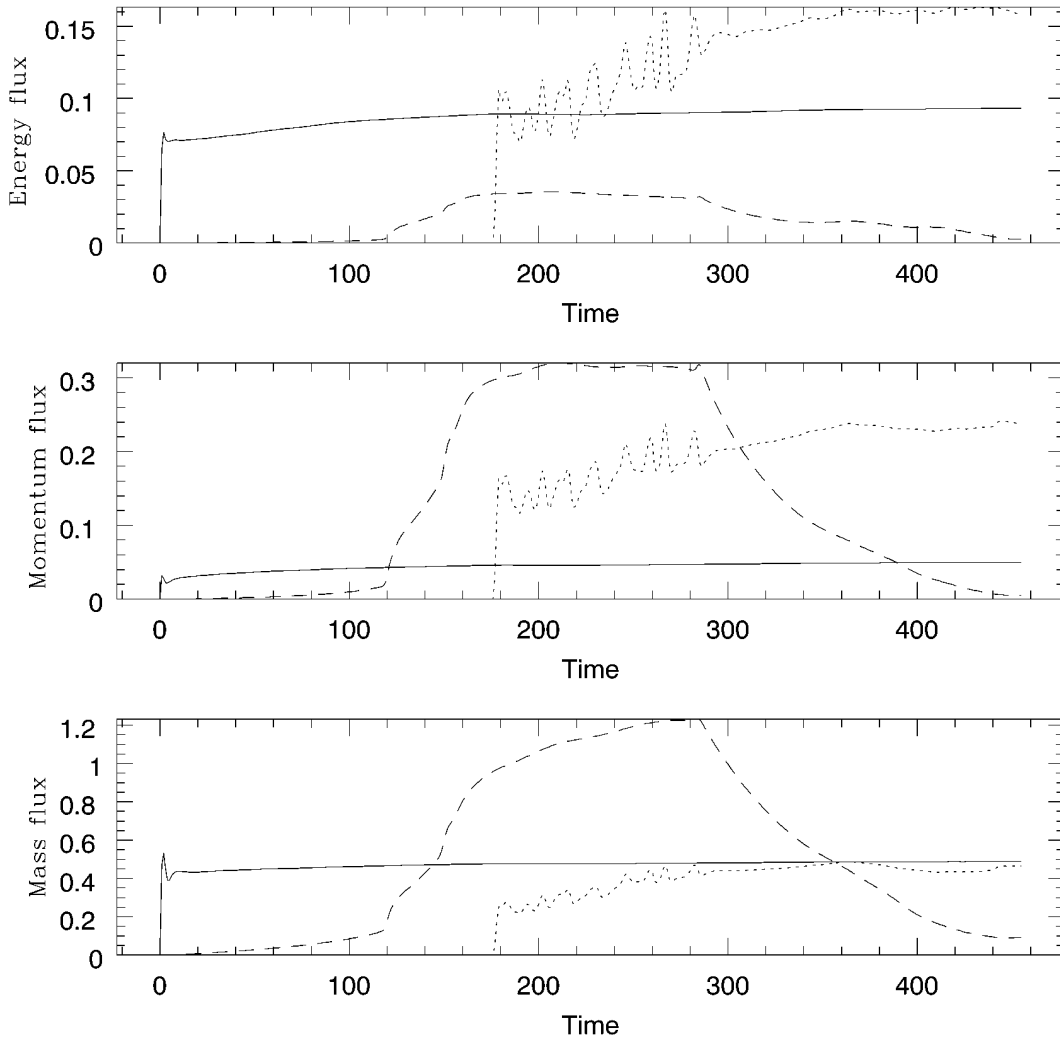


FIG. 11.—Here, we quantify the different fluxes carried by the jet. The bottom panel represents the mass flux, the middle panel represents the momentum flux, while the top panel represents the kinetic flux. The solid lines denotes the fluxes across the inner ($z = 0$) boundary. The short dashed lines denotes the fluxes across the outer radial boundary ($r = r_e$). Finally, the dotted lines denote the fluxes across the outer axial boundary ($z = z_e$) while the dashed lines denote the flux crossing the outer radial boundary. As the flow evolves in time, it gets more collimated until most of the flux crosses the outer axial boundary (dotted line).

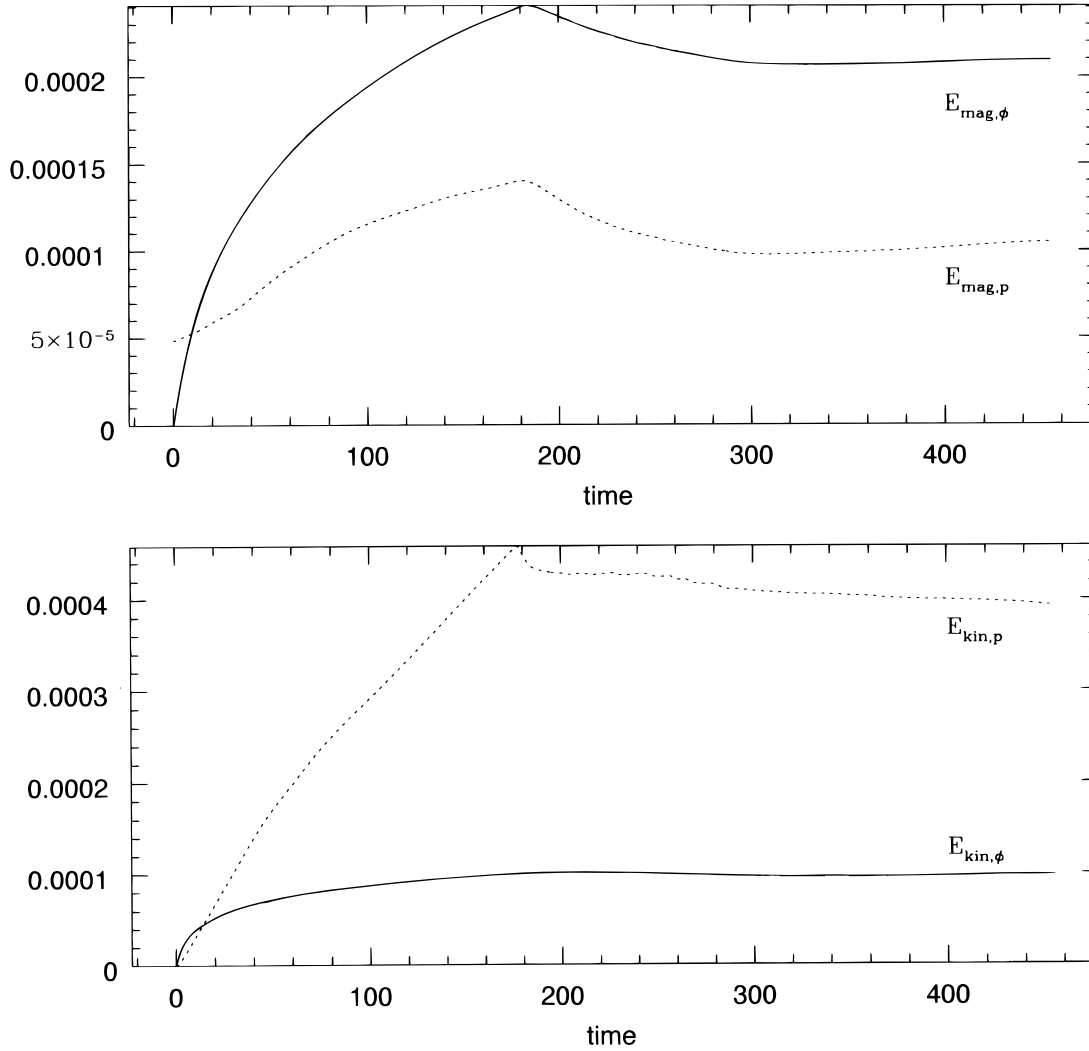


FIG. 12.—Quantification of the energies involved in the flow. In the upper/lower panel, the poloidal magnetic/kinetic energy is compared to the toroidal part.

0.1, condition (5.84) is then satisfied since

$$\frac{L_{\text{acc}}}{L_E} = 0.05 < 1. \quad (5.87)$$

Finally, in Figure 13, we show a snapshot (at $\tau = 400$) of the dependence of the mass outflow rate upon the poloidal velocity of the jet. The top panel shows that the velocity peaks at $r \simeq 6r_i$. The middle panel confirms the fact that most of the material is carried out between $3r_i < r_{\text{wind}} < 15r_i$. The lower panel indicates that the bulk of the material moves at speeds ($\simeq 0.6v_{K,i}$). Note that Figure 13 is taken at a snapshot time during which the highest velocities registered were only ($\simeq 0.8v_{K,i}$). However, velocities as high as $2.1v_{K,i}$ are reached in our flow.

6. SUMMARY AND CONCLUSIONS

We have presented 2.5-dimensional simulations of outflows accelerated from the surface of Keplerian accretion disks orbiting protostars or black holes. Our model is applicable for low-mass protostars and for the nonrelativistic regions of disks in AGNs accreting at sub-Eddington rates. In this paper, we have introduced the reader to our initial setup and our extended version of the ZEUS-2D

code. We have avoided the use of any softening parameter and have reduced the number of free parameters to five. The steady state outflow achieved in this simulation has properties that confirm many of the results of steady state, MHD wind theory. The acceleration of the flow from the disk occurs by a centrifugal effect whereby, at some point along sufficiently inclined field lines, centrifugal force dominates gravity and gas is flung away like “beads on a wire.” Thus, a toroidal field component is created because the field lines corotate with the underlying disk. The inertia of the matter in the flow region ultimately forces the field to fall behind the rotation of the disk, which produces the toroidal field component. This process is responsible for collimating the flow and enforcing its collimation far from the acceleration region near the disk and over the length of the jet.

Our main conclusions can be summarized as follows:

1. We found that collimation due to B_ϕ is always present in our simulations. A cylindrical configuration is always reached, as predicted by HN89. Our outflows rapidly achieve a highly collimated, even jetlike character.
2. The wind becomes super-Alfvénic and reaches *terminal velocities* of the order of $1-2v_{K,i}$. That is, an average velocity of $V_{\text{wind}} \sim 180 \text{ km s}^{-1}$ for our typical protostar, and of

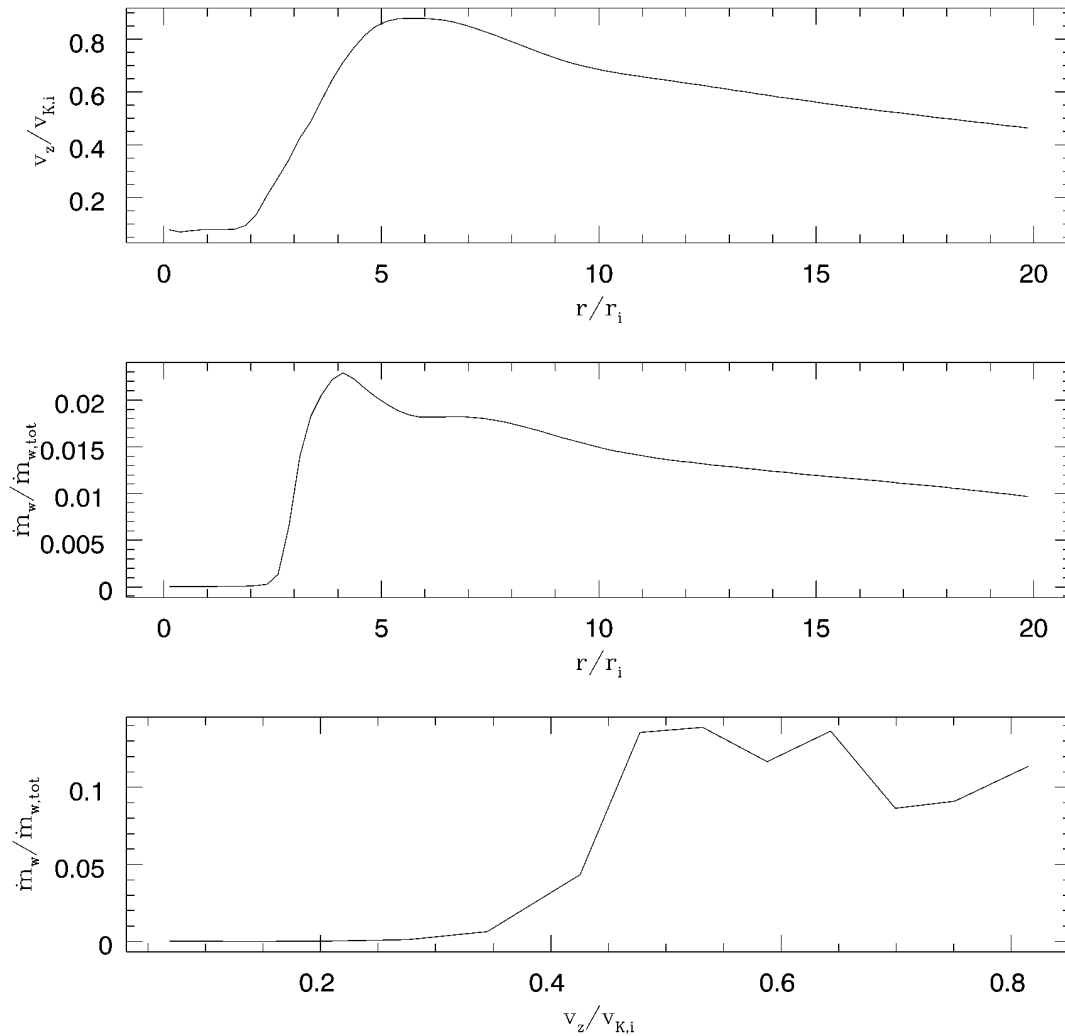


FIG. 13.—Snapshot (at $\tau = 400$) of the dependence of the mass outflow rate upon the poloidal velocity of the jet (*lower panel*). The top panel shows that the velocity peaks at $r \simeq 6r_i$. The middle panel shows size of the wind region ($3r_i < r_{wind} < 15r_i$).

about 10^5 km s^{-1} for a $10^8 M_\odot$ black hole.

3. Beyond the FM surface, the outflow is completely dominated by the so-called Hubble flow profile, $v_w \propto z$. Large-scale simulations will be important in determining whether or not such behavior persists on larger physical scales.

4. We find that κ and λ are simply related; $\lambda \simeq 2.4/\kappa^{2/3}$. The difference between the self-similar study (BP82 found $\lambda \simeq 1/\kappa$) and our result may be due to the different magnetic field distribution used.

5. Most of the energy in our outflow is shared between the bulk poloidal kinetic energy (2/3 of the total energy) and the toroidal magnetic energy (one-third of the toroidal energy).

6. In 1000 years, for example, and for our standard YSO, we estimate that our jetlike outflow carries a total energy of 3×10^{43} ergs sufficient to produce the observed molecular outflows (Lada 1985; Chernin & Masson 1991).

7. We found our flow to be very efficient in extracting energy from the disk since only a tiny part of the accreted gas needs to be converted into a wind. We estimate that the effective accretion rate through the underlying disk is $\dot{m}_a \simeq 6.0\dot{m}_w$. For the model parameters characterizing our simulation, the YSO accretes at a rate of about $5.5 \times 10^{-6} M_\odot \text{ yr}^{-1}$, while a $10^8 M_\odot$ black hole accretes at a rate of about

$0.1 M_\odot \text{ yr}^{-1}$. Our solution corresponds to an AGN with a sub-Eddington luminosity: $L/L_E = 0.05$.

Our conclusions must be tempered by emphasizing the assumptions we have made. For example, we have assumed axisymmetry and that the equation of state is polytropic. We have also assumed ideal MHD. The primary effect of reducing the dimensionality of the dynamics is to eliminate some modes of MHD instability. These modes can play an important role in the dynamics of outflows. It is clear that investigating the effects of the missing physics cited above is an important avenue for future research. While our present simulations show that the precepts of steady state MHD wind theory are essentially correct, nature, it seems, rarely chooses such solution. We present in an upcoming paper (Ouyed & Pudritz 1997) a magnetic configuration that gives rise to an episodic outflow.

We thank Jim Stone, David Clarke, and Patricia Monger for all their help and support during the course of this project and an anonymous referee for remarks that helped to clarify some of the discussion. R. O. acknowledges the financial support of McMaster University. The research grant of R. E. P. is supported by a grant from the Natural Science and Engineering Research Council of Canada.

REFERENCES

- Adams, F. C., Lada, C. J., & Shu, F. H. 1987, *ApJ*, 312, 788
- Appl, S., & Camenzid, M. 1992, *A&A*, 256, 354
- Balbus, S. A., & Hawley, J. F. 1991, *ApJ*, 376, 214
- . 1992, *ApJ*, 400, 610
- Beckwith, S. V. W., Sargent, A. I., Chini, R. S., & Güsten, R. 1990, *AJ*, 99, 924
- Bell, A. R., & Lucek, S. G. 1995, *MNRAS*, 277, 1327 (BL95)
- Blandford, R. D., & Payne, D. R. 1982, *MNRAS*, 199, 883 (BP82)
- Cabrit, S., & André, P. 1991, *ApJ*, 379, L25
- Camenzid, M. 1987, *A&A*, 184, 341
- Cao, X., & Spruit, H. C. 1994, *A&A*, 287, 80C
- Chandrasekhar, S. 1939, *Introduction to the Study of Stellar Structure* (Chicago: Univ. of Chicago Press)
- Chernin, L. M., & Masson, C. R. 1991, *ApJ*, 382, L93
- Clarke, D. A., Norman, M. L., & Burns, O. J. 1986, *ApJ*, 311, L63
- Courant, R., & Friedrichs, K. O. 1984, *Supersonic Flow and Shock Waves* (Berlin: Springer)
- Davis, C. J., Mundt, R., Eisloffel, J., & Ray, T. P. 1995, *AJ*, 110, 766
- Dewar, R. L. 1970, *Phys. Fluids*, 13, 2710
- Edwards, S., Ray, T. P., & Mundt, R. 1993, in *Protostars and Planets III*, ed. E. Levy & J. Lunine (Tucson: Univ. of Arizona Press), 567
- Eisloffel, J., & Mundt, R. 1992, *A&A*, 263, 292
- Esin, A. A., Narayan, R., & Ostriker, E. 1996, *ApJ*, 465, 312
- Ferreira, J., & Pelletier, G. 1995, *A&A*, 295, 807
- Frank, J., King, A. R., & Raine, D. J. 1992, *Accretion Power in Astrophysics* (Cambridge: Cambridge Univ. Press)
- Gilfanov, M. et al. 1995, in *The Lives of the Neutron Stars*, ed. M. A. Alpar, U. Kiziloglu, & J. van Paradijs (NATO ASI Series, 450) (Dordrecht: Kluwer), 331
- Hartigan, P. 1989, *ApJ*, 339, 987
- Hartigan, P., Raymond, J., & Meaburn, J. 1990, *ApJ*, 362, 624
- Hayashi, M. 1996, Ph.D. thesis, Chiba University, Japan
- Heyvaerts, J., & Norman, C. 1989, *ApJ*, 347, 1055 (HN89)
- Johnson, W. N., et al. 1994, in *The Second Compton Symposium*, ed. C. E. Fichtel, N. Gehrels, & J. P. Norris (New York: AIP), 515
- Kinzer, R. L., et al. 1994, in *The Second Compton Symposium*, ed. C. E. Fichtel, N. Gehrels, & J. P. Norris (New York: AIP), 531
- Königl, A. 1982, *ApJ*, 261, 115
- Königl, A. 1989, *ApJ*, 342, 208
- Königl, A., & Ruden, S. P. 1993, in *Protostars and Planets III*, ed. E. H. Levy & J. I. Lunine (Tucson: Univ. of Arizona Press), 641
- Lada, C. J. 1985, *ARA&A*, 23, 267
- Li, Z.-Y. 1995, *ApJ*, 444, 848
- Lind, K. R., Payne, D. G., Meier, D. L., & Blandford, R. D. 1989, *ApJ*, 344, 89
- Lovelace, R. V. E., Wang, J. C. L., & Sulkanen, M. E. 1987, *ApJ*, 315, 504
- McKee, C. F., & Zweibel, E. G. 1992, *ApJ*, 339, 551
- Mestel, L. 1989, in *Accretion Disks and Magnetic Fields in Astrophysics*, ed. G. Bekevedere (Dordrecht: Kluwer), 151
- Mouschovias, T. Ch., & Paleologou, E. V. 1980, *ApJ*, 237, 877 (MP80)
- Ouyed, R. 1996, Ph.D. thesis, McMaster Univ.
- Ouyed, R., & Pudritz, R. E. 1994a, *ApJ*, 419, 255
- . 1994b, *ApJ*, 423, 753
- . 1997, *ApJ*, in press
- Ouyed, R., Pudritz, R. E., & Stone, J. M. 1997, *Nature*, 385, 409
- Pelletier, G., & Pudritz, R. E. 1992, *ApJ*, 394, 117 (PP92)
- Pelletier, G., & Sol, H. 1992, *MNRAS*, 254, 635
- Pringle, J. E. 1981, *ARA&A*, 19, 137
- Pudritz, R. E., & Norman, C. A. 1986, *ApJ*, 301, 571
- Raga, A. C., & Kofman, L. 1992, *ApJ*, 386, 222
- Ray, T. P., & Mundt, R. 1993, in *Astrophysical Jets*, ed. M. Fall, C. O'Dea, M. Livio, & D. Burgarella (Cambridge: Cambridge Univ. Press), 145
- Reipurth, B., Raga, A. C., & Heathcote, S. 1992, *ApJ*, 332, 145
- Shibata, X., & Uchida, X. 1986, *PASJ*, 38, 631 (SU86)
- Shu, F. H. 1977, *ApJ*, 214, 488
- Shu, F. H., Adams, F. C., & Lizano, S. 1987, *ARA&A*, 25, 23
- Shu, F. H., Najita, J., Wilkin, F., Ruden, S. P., & Lizano, S. 1994, *ApJ*, 429, 781
- Sol, H., Pelletier, G., & Asseo, E. 1989, *MNRAS*, 237, 411
- Stone, J. M., & Norman, M. L. 1992a, *ApJS*, 80, 753 (SN92a)
- . 1992b, *ApJS*, 80, 791 (SN92b)
- . 1994, *ApJS*, 433, 746 (SN94)
- Uchida, Y., & Shibata, K. 1985, *PASJ*, 37, 515 (US85)
- Ustyugova, G. V., Koldoba, A. V., Romanova, M. M., Chechetkin, V. M., & Lovelace, R. V. E. 1995, *ApJ*, 439, L39 (U95)
- Wardle, M., & Königl, A. 1993, *ApJ*, 410, 218
- Zweibel, E. G., & McKee, C. F. 1995, *ApJ*, 439, 779